


Emergent mobility edges and intermediate phases in one-dimensional quasiperiodic plasmonic chains

Yizhi Hu ¹, Kun Yan ¹, and Xiaobin Chen ^{1,2,*}

¹*School of Science, State Key Laboratory on Tunable Laser Technology and Ministry of Industry and Information Technology Key Lab of Micro-Nano Optoelectronic Information System, Harbin Institute of Technology, Shenzhen, Shenzhen 518055, China*

²*Collaborative Innovation Center of Extreme Optics, Shanxi University, Taiyuan 030006, China*

 (Received 12 July 2023; revised 17 February 2024; accepted 21 February 2024; published 25 March 2024)

Anderson localization has been widely studied in low-dimensional aperiodic electronic, photonic, and acoustic systems. However, the disorder effect in the plasmonic system, where retardation and long-range couplings interact in complex ways, remains an open question. In this work, we investigate the localization properties of one-dimensional quasiperiodic plasmonic chains using the coupled dipole method and linearized Green's function. Our models, which incorporate nearest-neighbor or long-range dipole interactions, reveal localization transitions, mobility edges, and intermediate phases. It is found that long-range dipole interactions and non-Hermiticity due to retardation both play crucial roles in Anderson localization, yielding the emergence of intermediate phases with varying widths. A link between non-Hermiticity and Anderson transition is established by the mean phase rigidity, revealing strong non-Hermiticity along the phase boundary. The plasmonic model involving long-range interplay and retarded effect presents richer localization phenomena than the electronic counterpart that usually includes only nearest-neighbor coupling, laying a foundation for experimental observations of Anderson localization on plasmonic platforms.

DOI: [10.1103/PhysRevResearch.6.013322](https://doi.org/10.1103/PhysRevResearch.6.013322)

I. INTRODUCTION

Anderson localization, the phenomenon of the localization of electronic Bloch waves due to the presence of uncorrelated disorders, has long been the hot spot of theoretical and experimental investigation [1]. It is an underlying scattering mechanism behind metal-insulator phase transitions in three-dimensional (3D) solids. In one-dimensional (1D) and two-dimensional (2D) noninteracting systems, all eigenstates become localized as long as infinitesimal random disorder strengths are introduced in the thermodynamic limit [2,3]. In 3D, however, localized and extended states can coexist at different energies with critical energy separating localized and delocalized eigenstates, which is dubbed as the mobility edge [4,5]. While the typical Anderson transition occurs in 3D, a similar effect can be observed in 1D due to so-called quasidisorders [6–9]. The paradigmatic Aubry-Andr-Harper (AAH) model is a well-known case that exhibits a transition between a localized and an extended phase when the strength of the quasiperiodic potential exceeds a critical point determined by the self-duality condition [10–13]. By introducing short-range [14–16] and long-range hopping processes [17,18], or modified quasiperiodic potentials [19–21], various

extensions of the AAH model can possess energy-dependent mobility edges, resulting in intermediate phases where extended and localized states coexist [22–24]. Additionally, it has been discovered that in the presence of nonreciprocal hopping terms [25–28] or complex onsite potentials [29–31], the non-Hermitian AAH model can also exhibit mobility edges and undergo exotic localization transitions that coincide with topological phase transitions and/or real-complex transitions [29]. The recent advancements in the study of quantum gases of ultracold atoms trapped in optical lattices [32–34] have sparked a growing interest in the localization transition and the potential existence of mobility edges in quasiperiodic systems, leading to their experimental detections [23,35–37]. Despite extensive studies on Anderson localization transition across a plethora of domains such as electronics [38–40], photonics [41–43], and acoustics [44–46], explorations for this phenomenon in plasmonic systems remain limited owing to the intrinsic field leakage [47].

Surface plasmon polaritons are electromagnetic waves that propagate evanescently along a metal-dielectric interface, resulting from the coupling of the electric fields with the conduction electrons in the metal [48,49]. They can squeeze electromagnetic fields to subwavelength scales and enhance light-matter interactions at visible and near-infrared frequencies [50–53]. These waves can also be localized on the surfaces of metallic nanoparticles, where a localized surface plasmon (LSP) resonance between the electric field and electrons is formed, leading to strong near fields and large scattering cross sections [54,55]. Therefore, surface plasmon polaritons hold great potential in nanophotonic applications such as sensing [56–58], lasing [59], tuning of optical response [60,61],

*chenxiaobin@hit.edu.cn

Published by the American Physical Society under the terms of the Creative Commons Attribution 4.0 International license. Further distribution of this work must maintain attribution to the author(s) and the published article's title, journal citation, and DOI.

and radiative heat transport [62,63]. Furthermore, plasmonic systems, such as arrays of metallic nanoparticles that support surface plasmons, provide a powerful platform to mimic electronic tight-binding models and explore novel physics beyond the limitation of Fermi level and the complication of interacting particles [64–67]. They also embed interesting additional properties such as long-range interactions and non-Hermiticity. Recently, plasmonic analogies of topological electronic systems, including 1D and 2D Su-Schrieffer-Heeger models [68–70], honeycomb lattices [71–73], and breathing kagome lattices [74,75], have been proposed to investigate subwavelength topological edge, corner, and valley modes, along with energy transfer dominated by them. In addition to topological physics, the localization properties of plasmonic systems have been studied in various dipolar arrays, including geometries with random [76–79], quasirandom [80–82], and correlated random position orders [83,84]. Particularly, the Anderson localization of dipolar modes in plasmonic planar composites filled with random scatterers has been extensively studied [85]. However, there is still a lack of understanding regarding mobility edges and the resulting intermediate phases among these plasmonic eigenmodes.

In this work, we utilize a 1D quasiperiodic plasmonic dipolar array to mimic the incommensurate AAH model with off-diagonal modulation. By exploiting the coupled dipole method, which naturally incorporates full electromagnetic interactions, we investigate the Anderson localization in this quasiperiodic model. We first demonstrate the existence of intermediate phase hosting mobility edges in the quasistatic approximation. Then, to accurately capture the physical behavior of the plasmonic array, we include retarded effects and move to a non-Hermitian scheme, which results in the relaxation of localization, shift of phase boundary, and intermediate phases with all sorts of widths. Finally, we reveal the strong non-Hermiticity of dipole eigenmodes along the phase boundary with the aid of phase rigidity. Our findings not only shed light on the understanding of mobility edges and intermediate phases in the field of plasmonics, but also propose an alternative candidate for observing localization transitions and bound modes via photothermal probes in low dimensions.

The rest of the paper is organized as follows. In Sec. II, we introduce the quasi-1D model, the coupled dipole method, the linearized Green's function method, and some localization quantities. Afterward, we present and discuss the results in Sec. III. Finally, a conclusion is made in Sec. IV.

II. MODEL AND THEORY

A. Model

We consider a quasi-1D chain composed of spherical plasmonic nanoparticles aligned along the x axis (Fig. 1). The quasiperiodicity is introduced through incommensurate modulations of the spacings between nanoparticles as [15,86]

$$x_{n+1} - x_n = d[1 + \eta \cos(2\pi\beta n + \phi)], \quad (1)$$

where x_n is the position of the n th particle, d is the mean distance of every two adjacent particles, η is the amplitude of the incommensurate modulation, and β denotes an irrational number controlling the quasiperiodicity. Parameter ϕ

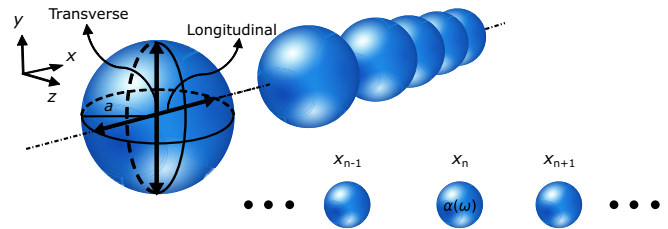


FIG. 1. Schematic plot of a quasiperiodic 1D InSb nanoparticle chain and decoupled polarizations of plasmonic modes. The nanoparticles in the chain are identical, characterized by a uniform radius a and polarizability $\alpha(\omega)$. The spacings between the nanoparticles are modulated by the Aubry-André-Harper model [Eq. (1)].

acts as a global phase shift of the modulation, which is crucial for topological edge states, but it does not affect localization properties [7]. Without loss of generality, we choose $\beta = (\sqrt{5} - 1)/2$ and $\phi = 0$ throughout the paper.

The nanoparticles in the chain are composed of doped InSb, which can be characterized by the electric dipole response due to the localized surface plasmon. This material exhibits localized plasmonic polariton resonances in the infrared region around $\omega_{\text{LSP}} = 1.7516 \times 10^{14}$ rad/s, with the permittivity described by the Drude model [70]

$$\varepsilon = \varepsilon_\infty \left[1 - \frac{\omega_p^2}{\omega(\omega + i\Gamma)} \right], \quad (2)$$

where ω is the angular frequency, $\varepsilon_\infty = 15.68$ is the high-frequency-limit permittivity, $\omega_p = 1.86 \times 10^{14}$ rad/s is the plasma frequency, and the damping constant $\Gamma = 1 \times 10^{12}$ rad/s accounts for Ohmic losses in a metal [87]. If the nanoparticle size is much smaller than the incident light's wavelength, i.e., in the quasistatic regime, then the InSb nanoparticles can be approximately regarded as electric dipoles according to Mie theory [88]. In this scenario, the optical response of an individual nanoparticle in the vacuum can be described by the quasistatic polarizability α_0 , which is given by [67]

$$\alpha_0 = 4\pi a^3 \varepsilon_0 \frac{\varepsilon - 1}{\varepsilon + 2}, \quad (3)$$

with particle radius a and vacuum permittivity ε_0 . To balance scattering and extinction, radiative correction to polarizability should be taken into account as follows [89]:

$$\alpha(\omega) = \frac{\alpha_0(\omega)}{1 + i\gamma\alpha_0(\omega)}, \quad (4)$$

where $k = \omega/c$ is the free-space wave number, $\gamma = -k^3/(6\pi\varepsilon_0)$ is the radiative loss, and c is the speed of light. It should be noted that the inclusion of radiative and Ohmic losses introduces non-Hermiticity into the plasmonic system. However, we expect that this non-Hermiticity imposed by damping only determines the quality factor of leaky modes, and does not alter their spatial localization natures [81]. In addition, the modified long-wavelength approximation [90,91], originating from the dynamic depolarization due to retardation, is incorporated into the polarizability commonly, and it can cause a redshift of the dipole resonances, which increases

as the nanoparticle grows larger, but this effect does not correct the spatial distribution of dipole modes either.

B. Coupled dipole method

If a system of nanoparticles is sufficiently spaced such that radius a and nearest-neighbor spacing d satisfy $d > 3a$, each nanoparticle can be treated as a point dipole validly [92]. A nanoparticle at position \mathbf{r}_n with polarizability α supports a dipole moment \mathbf{p}_n when excited by an external electric field. For a lattice of nanoparticles, a coupled dipole equation can be written to describe the dipole moment of a nanoparticle induced by an external field and the sum of all neighboring dipole moments [67]

$$\frac{1}{\alpha(\omega)}\mathbf{p}_n = \mathbf{E}(\mathbf{r}_n) + \frac{k^2}{\varepsilon_0} \sum_{n' \neq n} \mathbf{G}(\mathbf{r}_n - \mathbf{r}_{n'}, \omega) \mathbf{p}_{n'}, \quad (5)$$

where \mathbf{p}_n is the dipole moment at site n , $k = \omega/c$, $n' \in \{1, 2, \dots, N\}$, N is the number of the nanoparticles, $\mathbf{E}(\mathbf{r}_n)$ is the incident electric field at site n , and \mathbf{G} is the free-space dyadic Green's function describing the interactions between point dipoles, which is given by [89]

$$\mathbf{G}(\mathbf{r}_n - \mathbf{r}_{n'}, \omega) = \frac{\exp(ikr)}{4\pi r} \left[\left(\frac{i}{kr} - \frac{1}{k^2 r^2} + 1 \right) \mathbf{I} + \left(-\frac{3i}{kr} + \frac{3}{k^2 r^2} - 1 \right) \hat{\mathbf{r}} \otimes \hat{\mathbf{r}} \right] \quad (6)$$

with $r = |\mathbf{r}| = |\mathbf{r}_n - \mathbf{r}_{n'}|$ being the distance between two nanoparticles and $\hat{\mathbf{r}} = \mathbf{r}/r$ being the unit vector parallel to \mathbf{r} . Note that \mathbf{I} is an identity matrix and the symbol \otimes represents the Kronecker product. For this quasiperiodic 1D array, there are two types of electromagnetic modes, including longitudinal (x) and transverse (y or z) ones. In this way, Green's functions can be decoupled into the longitudinal and transverse mode parts as

$$G_{xx}(x, \omega) = \frac{2e^{ikx}}{4\pi k^2 x^3} (1 - ikx), \quad (7)$$

$$G_{yy/zz}(x, \omega) = \frac{-e^{ikx}}{4\pi k^2 x^3} (1 - ikx - k^2 x^2). \quad (8)$$

For the longitudinal polarization, the Green's function [Eq. (7)] can be broken up into near-field and intermediate-field components, which decay at $1/x^3$ and $1/x^2$ rates individually. The third term in the transverse Green's function [Eq. (8)] is the far-field term and can be regarded as long-range interaction since it decays as $1/x$ resembling the Coulomb potential. In the quasistatic approximation, neglecting retardation by taking the limit of $kd \rightarrow 0$, Green's functions can be further simplified to

$$G_{xx}^{QS}(x, \omega) = \frac{2}{4\pi k^2 x^3}, \quad (9)$$

$$G_{yy/zz}^{QS}(x, \omega) = -\frac{1}{4\pi k^2 x^3}. \quad (10)$$

In this regime, it can be inferred from Green's functions that the interaction between collective dipoles is governed by the near-field term that decays as $1/x^3$. In addition, to determine the spectral response of a finite array of nanoparticles, we

can set the incident field \mathbf{E} to be zero, and then solve the eigenvalue equation [Eq. (5)] [93].

C. Linearized Green's function

In order to fully capture the non-Hermitian behavior of the plasmonic chain, we can utilize the linearized Green's function method to incorporate the retarded interactions. However, when the full Green's function and radiative polarizability are used, the coupled dipole equation of the system becomes a nonlinear eigenvalue problem. Calculating the eigenmodes of this system in the nonlinear regime requires searching for zeros in the complex plane, which can be computationally demanding. To avoid this difficulty, we can linearize the dyadic Green's function by letting $\omega = \omega_{\text{LSP}}$ and removing the ω dependence of the Green's function as follows ($v = x, y, z$) [67]:

$$E p_{v,n} = \frac{d^3}{\alpha(\omega)} p_{v,n} = \frac{k_{\text{LSP}}^2}{\varepsilon_0} \sum_{n' \neq n} \tilde{G}_{vv}(\tilde{x}_{nn'}) p_{v,n'}, \quad (11)$$

with

$$\begin{aligned} \tilde{G}_{xx}(\tilde{x}_{nn'}) &= \frac{2e^{ik_{\text{LSP}}d\tilde{x}_{nn'}}}{4\pi k_{\text{LSP}}^2 \tilde{x}_{nn'}^3} [1 - ik_{\text{LSP}}d\tilde{x}_{nn'}], \\ \tilde{G}_{yy/zz}(\tilde{x}_{nn'}) &= \frac{-e^{ik_{\text{LSP}}d\tilde{x}_{nn'}}}{4\pi k_{\text{LSP}}^2 \tilde{x}_{nn'}^3} [1 - ik_{\text{LSP}}d\tilde{x}_{nn'} - (k_{\text{LSP}}d)^2 \tilde{x}_{nn'}^2], \end{aligned} \quad (12)$$

where $\tilde{x}_{nn'} = |x_n - x_{n'}|/d$ is the spacing between two nanoparticles scaled by d and $k_{\text{LSP}} = \omega_{\text{LSP}}/c$ is regarded as the magnitude of the wave vector of light with the same frequency as the single-particle surface plasmon resonance. The symbols n and n' label the nanoparticle site. We can then diagonalize the linearized Green's matrix to obtain the eigenpairs E and \mathbf{p} . Additionally, we can find the eigenfrequencies of the modes by letting $E = d^3/\alpha(\omega)$ and then solving for ω , which is a valid approximation for small nanoparticles. This is because the frequency in the polarizability varies more rapidly than the frequency in the Green's function [94]. Although the approximation is less valid for larger nanoparticles, particularly at the light line, it still allows us to touch the boundary of the large-particle scheme. Note that the solved eigenfrequencies are commonly represented in the complex form of $\omega = \text{Re}(\omega) + i \text{Im}(\omega)$, where the real part $\text{Re}(\omega)$ encapsulates the natural frequency of a plasmonic eigenmode, and the imaginary part $\text{Im}(\omega)$ provides insight into its decay rate. To assess the quality of a specific mode, we can examine the mode quality, which is defined as the inverse of the magnitude of $\text{Im}(\omega)$, i.e., $1/|\text{Im}(\omega)|$. A high value of $1/|\text{Im}(\omega)|$ indicates a favorable mode quality for the corresponding eigenmode.

D. Localization quantities

In order to measure the localization nature of states in the quasiperiodic plasmonic chain, we study the inverse and normalized participation ratios of our system. The presence of an intermediate phase, for which phase localized and extended eigenmodes coexist in the spectrum, can be demonstrated by simultaneously calculating the mean inverse participation ratio (IPR) and the mean normalized participation ratio (NPR)

TABLE I. Values of $\langle \text{IPR} \rangle$, $\langle \text{NPR} \rangle$, and Δ for localized, extended, and intermediate phases in a 1D disordered chain with N nanoparticles.

Phase	$\langle \text{IPR} \rangle$	$\langle \text{NPR} \rangle$	Quantity Δ
Localized	$\sim O(1)$	$\sim N^{-1}$	$\Delta < -\log_{10} N$
Extended	$\sim N^{-1}$	$\sim O(1)$	$\Delta < -\log_{10} N$
Intermediate	$\sim O(1)$	$\sim O(1)$	$-2 \lesssim \Delta \lesssim -1$

of the eigenmodes [23]. For the l th dipole eigenmode p_n^l , they are defined as [22]

$$\text{IPR}^l = \frac{\sum_{n=1}^N |p_n^l|^4}{\left(\sum_{n=1}^N |p_n^l|^2\right)^2}, \quad \text{NPR}^l = \left[N \sum_{n=1}^N |p_n^l|^4\right]^{-1}, \quad (13)$$

where N is the size of the lattice, and the sum is over the lattice sites denoted by n . Furthermore, by averaging these two quantities over all eigenmodes, we can define the mean IPR and NPR of the plasmonic system:

$$\begin{aligned} \langle \text{IPR} \rangle &= \frac{1}{N} \sum_{l=1}^N \text{IPR}^l, \\ \langle \text{NPR} \rangle &= \frac{1}{N} \sum_{l=1}^N \text{NPR}^l. \end{aligned} \quad (14)$$

Generally, we have $\langle \text{IPR} \rangle \sim N^{-1}$ or $O(1)$ if the eigenmode is an extended or localized mode, respectively. As for $\langle \text{NPR} \rangle$, we can conclude a contrary interpretation, i.e., $\langle \text{NPR} \rangle \sim O(1)$ or N^{-1} if the eigenmode is an extended or localized mode, respectively. Moreover, we define the intermediate phase as the regimes in which $\langle \text{IPR} \rangle$ and $\langle \text{NPR} \rangle$ are finite in the thermodynamic limit ($N \rightarrow +\infty$). To figure out whether the intermediate, fully extended, and localized phases exhibit in the system conveniently, we calculate the quantity Δ as [95]

$$\Delta = \log_{10}[\langle \text{IPR} \rangle \times \langle \text{NPR} \rangle]. \quad (15)$$

When the values of both $\langle \text{IPR} \rangle$ and $\langle \text{NPR} \rangle$ are finite, we get $-2 \lesssim \Delta \lesssim -1$. Specifically, we have $\Delta < -\log_{10} N$ when either of them is $\sim N^{-1}$. For convenience, we conclude the typical orders of $\langle \text{IPR} \rangle$, $\langle \text{NPR} \rangle$, and the main range of Δ for different phases in Table I.

III. RESULTS AND DISCUSSION

A. Quasistatic regime

We first investigate the plasmonic AAH model for a small chain geometry ($a = 50$ nm, $d = 1$ μ m) with $N = 100$ nanoparticles under the quasistatic approximation and discuss how the localization properties vary as a function of the disorder modulation amplitude η . To recognize the effect of full pair dipole interactions, we account for only the nearest-neighbor (NN) interactions and omit the higher-order interplay artificially to make an approximate model. We force the model to be chiral and then compare it with the physical full-dipole (FD) model. In this regard, we display the mean IPR and NPR of all transverse eigenmodes with increasing values of η for these two different cases, i.e., NN and FD

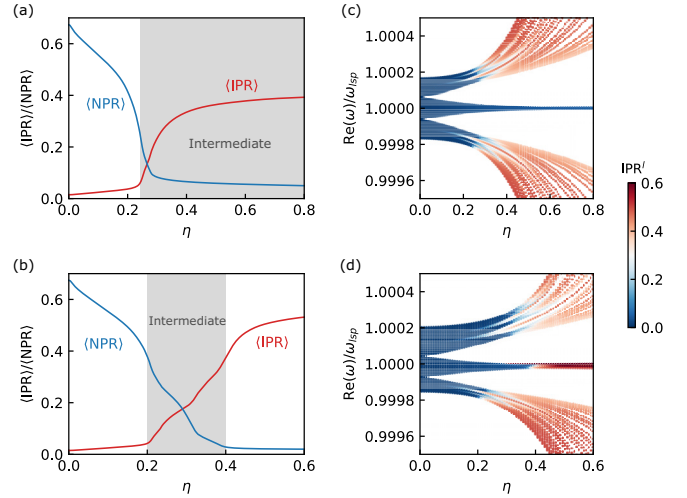


FIG. 2. Mean inverse participation ratio ($\langle \text{IPR} \rangle$, red lines) and mean normalized participation ratio ($\langle \text{NPR} \rangle$, blue lines) of transverse eigenmodes as a function of the modulation amplitude η under the quasistatic regime considering (a) the nearest-neighbor and (b) full-dipole interactions. The gray-shaded regions suggest the intermediate phases. (c), (d) The real parts of the eigenfrequency spectra versus η with the nearest-neighbor and full-dipole interactions, respectively. The colors are rendered with their respective IPR values. The material parameters for the InSb nanoparticle chain are set as $a = 50$ nm, $d = 1$ μ m, and $N = 100$.

interactions in Figs. 2(a) and 2(b), respectively. We can see that there exist three distinct phases depending on the modulation amplitude η . In the case of FD interactions, showed in Fig. 2(b), when η is smaller than the threshold $\eta_{c1} \approx 0.2$, all the eigenmodes are extended, as indicated by a vanishing IPR. Each of the eigenmodes is localized, as suggested by a finite IPR when η exceeds the second threshold $\eta_{c2} \approx 0.4$. When η lies in-between two thresholds (gray-shaded region), an intermediate regime hosting a mobility edge characterized by the coexistence of extended and localized states shows up. This mobility edge, also known as the hierarchy of localization transitions, is driven by the intrinsic full dipole-dipole interactions of the plasmonic system exactly. It is interesting to note that, differing from the electronic AAH model with a diagonal modulation, even for very large η values the NN case still cannot enter the regime where all eigenmodes are localized [Fig. 2(a)]. Hence, the NN plasmonic system exhibits an ultrawide intermediate phase for $\eta > \eta_c \approx 0.25$. We stress that the ultrawide intermediate phase observed in the plasmonic systems is not caused by finite-size effects. To rule out this possibility, we perform the remaining finite values of $\langle \text{IPR} \rangle$ and $\langle \text{NPR} \rangle$ for different system sizes described by a sequence of Fibonacci numbers when η is above η_c in Appendix A. The results clearly indicate the existence of the ultrawide intermediate phase even in ultralong nearest-neighbor plasmonic systems.

To reveal the mechanisms and mobility edges behind the ultrawide intermediate phase clearly, we plot all the transverse eigenfrequencies encoded with the corresponding IPR for the above two cases as shown in Figs. 2(c) and 2(d). For clarity, we normalize the frequency in a unit of ω_{LSP} and depict only

the spectra within a normalized frequency window of [0.9995, 1.0005]. After a comparison with the case considering the FD interactions as presented in Fig. 2(d), it is found that the spectral structure under the NN approximation [Fig. 2(c)] is almost symmetric with respect to ω_{LSP} and the IPR distribution of the eigenmodes is also symmetric, which is enforced by the chiral symmetry of the NN system. An asymmetric spectrum, as well as an asymmetric IPR distribution, due to the breaking of chiral symmetry introduced by full dipole-dipole interactions, is exhibited in the circumstance of the FD interactions, which can be observed in a series of modified electronic AAH models with higher-order hopping terms [14,17,27]. Moreover, the spectral gaps at specific band fillings l/N separate different band sets and correspond to different topological numbers (see Appendix C for details), where l is the mode index, and N is the total number of modes or sites. We also find that the IPR of all three main bands separated by two gaps with fillings β and $1 - \beta$ exhibits a higher value with η beyond a critical value in both cases, but the critical value shifts with the frequencies if considering the FD interactions, which exactly suggests a mobility edge. However, we note that all the main bands in the NN case undergo sharp localization transitions at the critical point $\eta_c \approx 0.25$ but the moderate main bands around ω_{LSP} , corresponding to $1 - \beta < l/N < \beta$, which could result in two symmetric mobility edges dividing the spectrum into a hierarchy where extended eigenmodes appear in the middle while the localized ones appear near two edges (see an analytical solution in Appendix B) and the ultrawide intermediate phase as demonstrated in Fig. 2(a).

To gain a more insightful visualization of the transition between the extended and localized phases in both the NN and FD cases, it is beneficial to examine the IPR distributions of the individual eigenmodes identified by the filling indices l/N , as depicted in Figs. 3(a) and 3(b). The deep blue patch in Fig. 3(a) for $\eta > 0.25$ corresponds to the never localized eigenmodes within the filling range of $1 - \beta < l/N < \beta$ in the NN case. By contrast, there is a transition to the localized phase through the critical value $\eta_{c_2} \approx 0.4$ for these eigenmodes in the FD case [see Fig. 3(b)]. This crucial difference corroborates the emergence of the ultrawide intermediate phase in the NN case. We further confirm the existence of the ultrawide intermediate phase by inspecting the spatial distribution of the dipole eigenmode at $l/N = 0.5$ with fixed η ranging from 0.1 to 0.8 for these two cases. It can be seen from Figs. 3(c) and 3(d) that localized and extended modes have different forms of dipole moments. The dipole eigenmode becomes rugged as η increases but is extended over the whole chain for both cases at $\eta < 0.4$. However, for the FD case, the mode shows a sharp transition once $\eta > 0.4$ and turns to localize on a few lattice sites, while the mode is always extended for the NN case.

B. Fully retarded regime

Within the quasistatic approximation, our investigation focuses mainly on transverse polarization. It is worth noting that for longitudinal eigenmodes, the frequency spectrum and band gaps are substantially wider due to the presence of stronger dipole-dipole couplings, characterized by G_{xx}^{QS} [Eq. (9)]. Despite this difference, the localization hierarchy

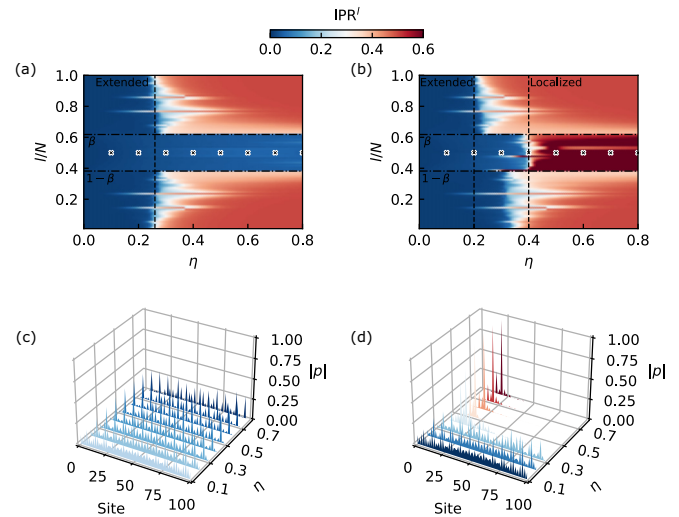


FIG. 3. Inverse participation ratio (IPR) associated with the filling indices l/N as a function of the disorder amplitude η for a chain of $N = 100$ InSb nanoparticles with $a = 50$ nm and $d = 1$ μm under the quasistatic regime considering (a) nearest-neighbor and (b) full-dipole interactions. The black dashed vertical lines indicate the critical phases, while the black dotted horizontal lines separating the band sets denote the fillings of $l/N = \beta$ and $1 - \beta$. (c), (d) The spatial distribution of dipole moment intensities for those modes marked by black diagonal cross markers in (a) and (b), respectively, with varying η from 0.1 to 0.8. Colors in (a) and (b) are rendered by IPR of each eigenmode.

of the longitudinal modes is almost identical to that of the transverse modes. However, we expect a notable discrepancy between these two polarizations in the retarded regime due to the distinct decay terms between Eqs. (7) and (8). With the retarded effect incorporated, non-Hermiticity manifests in the quasiperiodic plasmonic model, hence, in the following, we turn to investigate the impact of the retardation-induced non-Hermiticity on the Anderson localization of this model.

The mean IPR of the longitudinal (LO) and transverse (TR) eigenmodes with the NN or FD interactions in the retarded regime are displayed in Fig. 4. Here, $\kappa = k_{\text{LSP}}d/\pi$ is a tuning parameter, which can be varied by changing the mean distance between nanoparticles, of the retarded effect. The case of $\eta = 0.15$ shown in Fig. 4(a) reveals that a large part of the longitudinal and transverse eigenmodes are extended, with the mean IPRs for both NN and FD cases over the entire eigenmodes in a system of $N = 1000$ showing fairly low values at the $\kappa = 0$ limit. When $\kappa > 0$, under the retarded effect, the longitudinal eigenmodes with both interactions are disturbed, leading to the delocalization of initially localized modes on the disordered chain, driving the plasmonic system with longitudinal polarization toward a more extended phase as a whole. The trend continues until $\kappa \approx 0.8$, beyond which the extended modes in the longitudinally polarized system gradually return to being localized due to the decoupling between the dipoles. However, the localization behavior of the transverse eigenmodes is rather complicated for the small η of 0.15. For $0 < \kappa < 0.28$, the mean IPR of transverse eigenmodes in the NN case forms a broad peak, slightly exceeding the counterpart at $\kappa = 0$. After $\kappa = 0.28$, it varies in the same way as the

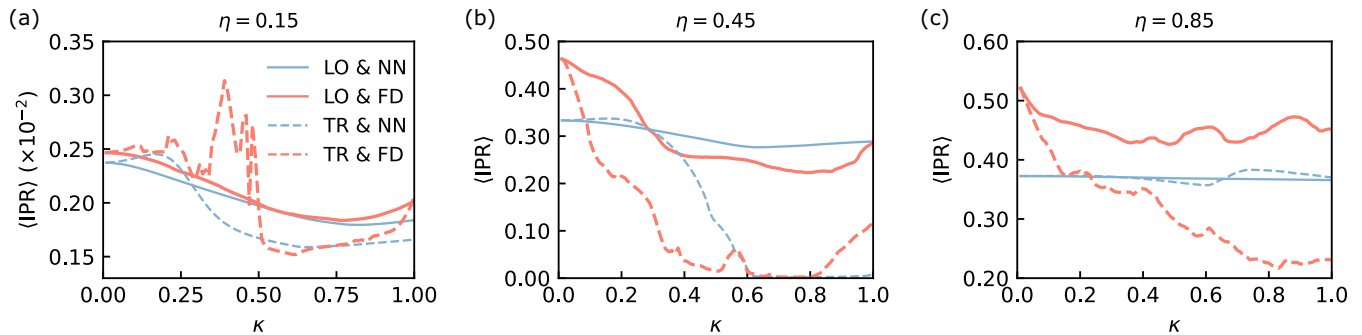


FIG. 4. Mean inverse participation ratios ($\langle \text{IPR} \rangle$) of the longitudinal (LO) and transverse (TR) eigenmodes for a chain of $N = 1000$ InSb nanoparticles as a function of the tuning parameter κ for modulation amplitude (a) $\eta = 0.15$, (b) $\eta = 0.45$, and (c) $\eta = 0.85$. The results obtained from both nearest-neighbor (NN) and full-dipole (FD) interactions are compared.

longitudinal modes. Furthermore, the $\langle \text{IPR} \rangle$ curve of eigenmodes for transverse polarization in the FD case exhibits a series of local peaks in the interval of $\kappa \in (0, 0.5)$, particularly the towering peaks after $\kappa > 1/\pi \approx 0.32$ (for $k_{\text{LSP}}d > 1$), which may be attributed to the presence of abnormal edge modes induced by far-field interactions at large spacings [94].

Similarly, for a moderate η value of 0.45 given in Fig. 4(b), some localized modes of longitudinal polarization (solid lines) in the cases of NN and FD become extended again and then relocalized with increasing κ . Despite this modulation due to retardation, the localization profiles of the longitudinally polarized system, characterized by $\langle \text{IPR} \rangle$, are only mildly affected. In the small η case ($\eta = 0.15$), the retarded effect represented by κ has a more pronounced impact on the localization properties of the transverse modes. Thus, a similar behavior can be expected even when η is not small. As can be seen from the $\langle \text{IPR} \rangle$ plot of transverse eigenmodes for the NN and FD cases [dashed lines in Fig. 4(b)], the values of $\langle \text{IPR} \rangle$ drop dramatically as κ increases and down to 0 at $\kappa = 0.6$ eventually, because all NN couplings are mediated by the far-field terms when κ is above 0.6. Additionally, for the FD case, the $\langle \text{IPR} \rangle$ plot has two curious turning points near $\kappa \approx 0.56$ and 0.8.

For a larger η value of 0.85 given in Fig. 4(c), one can see that both cases of NN and FD get high values of $\langle \text{IPR} \rangle$ at the beginning, indicating the localization of most modes in the presence of strong disorder. Furthermore, when the system is subjected to retardation, the $\langle \text{IPR} \rangle$ value of the eigenmodes, excluding the transverse FD case, fluctuates around the initial value observed at $\kappa = 0$. It is worth noting that there exists a region in the transverse NN case where the $\langle \text{IPR} \rangle$ value gradually ascends and eventually surpasses the value at $\kappa = 0$ after κ reaches approximately 0.6.

The features of $\langle \text{IPR} \rangle$ at various levels of disorder η can be further understood by checking the IPR distributions for each individual eigenmode (IPR^l). For $\eta = 0.45$, we take the transverse-polarized eigenmodes with NN and FD interactions and depict their IPR^l in Figs. 5(a) and 5(c), respectively. We successively define different blocks of IPR^l by black dotted lines for $l/N = [\{3(1 - \beta)\}, \{2\beta\}, 1 - \beta, \beta, \{4\beta\}, \{4(1 - \beta)\}, 2(1 - \beta), \{3\beta\}]$ with $\{\cdot\}$ being the fractional part of a real number, and each of these fillings corresponds to a gap between sets of eigenfrequency bands as illustrated in Appendix C. From Fig. 5(a), it is clear that all localized modes

are destroyed after $\kappa = 0.6$, which means that the plasmonic system is fully extended ($\langle \text{IPR} \rangle \sim 0$) when $\kappa > 0.6$. Nonetheless, once taking the FD interactions, the system hosts two bright patches appearing in Fig. 5(c) for $0.5 < \kappa < 0.6$ and $\kappa > 0.8$, indicating that some of the extended modes become localized abruptly near $\kappa \approx 0.56$ and 0.8. These observations are consistent with the behavior of the transverse mode with the NN and FD interactions in Fig. 4(b). We also observe that, for the NN case in Fig. 5(a), the localized-to-extended edge goes up (down) in steps as l/N increases (decreases) with κ for $l/N > \beta$ ($l/N < 1 - \beta$), which implies that the retardation can exhibit a new mobility edge resembling the role of quasiperiodic disorder. The FD case shown in Fig. 5(c) also presents a similar localized-to-extended mobility edge compared to the extended-to-localized edge under the quasistatic regime but a reverse transition priority before $\kappa = 0.32$. For $\kappa > 0.32$, however, the *in situ* localization hierarchy is overturned by the retarded long-range interactions.

For $\eta = 0.8$, Fig. 5(b) shows that the originally extended modes for $1 - \beta < l/N < \{4\beta\}$ and $\{4(1 - \beta)\} < l/N < \beta$ start to get localized when $\kappa > 0.6$ for the NN case. Specifically, the $\langle \text{IPR} \rangle$ value for the FD case decreases significantly as κ increases, which stems from Fig. 5(d) that the originally localized modes are significantly affected and delocalized gradually by the retarded long-range term in the transverse Green's function. We also see that both band sets for $l/N > \beta$ and $l/N < 1 - \beta$ in different blocks and within the same blocks show nonuniform delocalization transitions. This fact can be explained by the subdivision of the enlarged minigaps within the same band set into multiple subsets at the strong disorder level of $\eta = 0.85$. The above examples demonstrate that the localization properties of our plasmonic chain, when combined with retarded effects, generally exhibit a nontrivial and nonmonotonic dependence on the retardation parameter κ .

Having studied the impact of the retardation parameter κ on the localization property of the plasmonic chain, we now uncover the effect of varying η with different κ . In the limit of $\kappa = 0$, which corresponds to the quasistatic regime as shown in Fig. 2, the behavior of the plasmonic system is distinct for the NN and FD cases as the disorder strength η varies. When η is below the critical point, both NN and FD cases exhibit extended modes. However, when η is beyond the critical point, the modes in the NN case become partially localized. On the

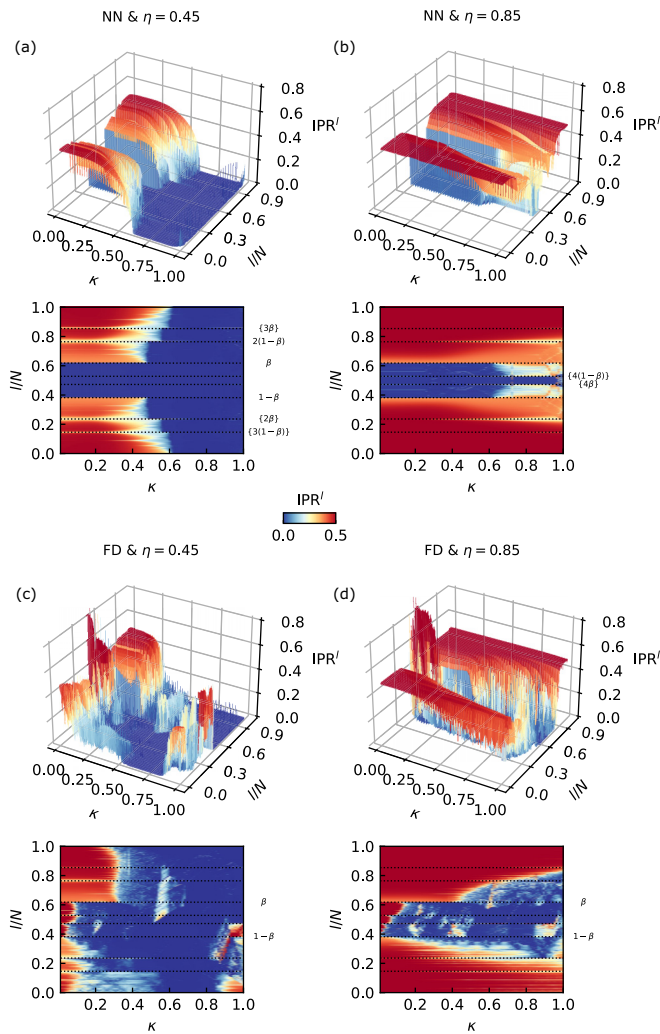


FIG. 5. Inverse participation ratios (IPRs) of each individual transverse eigenmode with increasing κ under different values of η and interaction types. Specifically, four distinct scenarios are considered: (a) nearest-neighbor interactions with $\eta = 0.45$, (b) nearest-neighbor interactions with $\eta = 0.85$, (c) full-dipole interactions with $\eta = 0.45$, and (d) full-dipole interactions with $\eta = 0.85$. The 2D contour plots at the lower panels are projections of the corresponding 3D surface graphs. In the contour plots, the black dotted lines represent the band separations corresponding to the gap indices of $\{[3(1-\beta)], [2\beta], 1-\beta, \beta, [4\beta], [4(1-\beta)], 2(1-\beta), [3\beta]\}$. Note that both the heights and the colors of the 3D plots change according to the value of IPR' .

other hand, by considering the FD interactions and further increasing η , the modes become completely localized. As a result, in the special limit of $\kappa = 0$, the plasmonic system displays different mobility edges and intermediate phases in these two distinct scenarios. That is exactly the moral of the story in the quasistatic regime. Now, we can proceed to study how the localization property of the plasmonic system changes with varying η under a fixed value of κ .

In Fig. 6, we plot $\langle \text{IPR} \rangle$ and $\langle \text{NPR} \rangle$ as a function of η with three given κ for different polarizations and interactions. When κ is small ($\kappa = 0.1$), the appearance of localized modes, mobility edge, and intermediate phase for all cases is in accord with that discovered in the quasistatic scenario

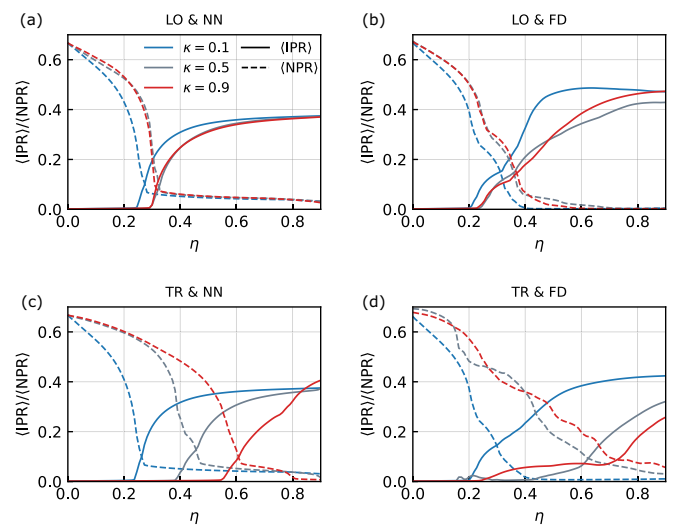


FIG. 6. The mean inverse participation ratio ($\langle \text{IPR} \rangle$, solid lines) and mean normalized participation ratio ($\langle \text{NPR} \rangle$, dashed lines) of the eigenmodes vary with η , while κ is fixed at 0.1 (blue lines), 0.5 (gray lines), and 0.9 (red lines) for four different cases: (a) longitudinal polarization with nearest-neighbor interactions (LO and NN), (b) longitudinal polarization with full-dipole interactions (LO and FD), (c) transverse polarization with nearest-neighbor interactions (TR and NN), and (d) transverse polarization with full-dipole interactions (TR and FD).

(Fig. 2). In contrast, when κ takes a larger value ($\kappa = 0.5$), there are several significant changes. First, for longitudinal polarization, not only the localized modes with the NN interactions but also the ones with the FD interactions appear at a marginally larger η value [Figs. 6(a) and 6(b)], which can be attributed to the fact that higher-order hoppings are small enough at the moderate κ for the FD case. Yet, in the transverse case, the critical value for the debut of localized modes with the NN interactions increases apparently, as presented by the gray lines in Fig. 6(c). If the long-range term is introduced [Fig. 6(d)], there is a plateau in the $\langle \text{IPR} \rangle$ curve before most modes turn to be localized, and a double-hump around $\eta \approx 0.18$, resembling the one observed in Fig. 4(a). Second, in the case of longitudinal and transverse polarizations, the ultrawide intermediate phase manifesting under the NN interactions still exists. However, with the long-range hopping allowed, the region of the intermediate phase with finite width expands a little bit for the longitudinal polarization, while the transverse modes feature a much wider intermediate phase since the long-range term gets notable. Last, a more extended phase merges at $\eta = 0$ as reflected by a higher $\langle \text{NPR} \rangle$ for the transverse FD case, which can be understood by the fact that the effective interferences between electromagnetic waves generated by collective plasmons and photons would broaden the spatial distribution of dipole moments for certain modes, albeit the position order is periodic. As κ increases further to $\kappa = 0.9$, we see that except for the narrower intermediate phase under the long-range interactions, there is no important change in longitudinally polarized modes. Likewise, there also hosts a plateau and a very wide but shifted intermediate phase in the transverse FD case. Meanwhile, a lower $\langle \text{NPR} \rangle$ is discovered at $\eta = 0$, implying the nonmonotonic tuning

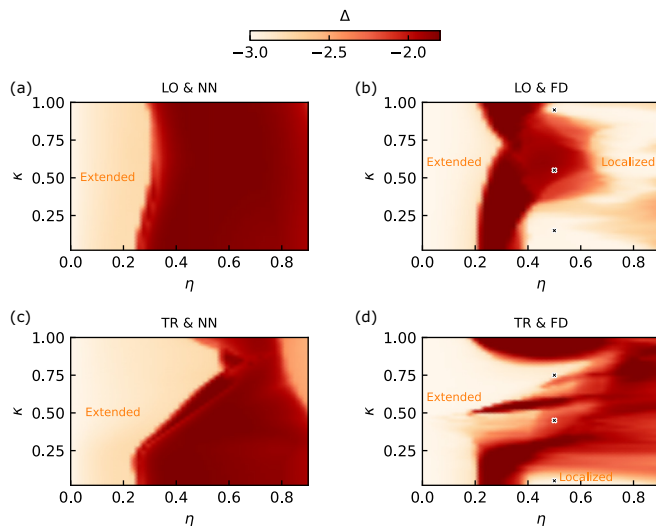


FIG. 7. The localization phase diagrams of an $N = 1000$ InSb-nanoparticle quasiperiodic chain for four different cases: (a) longitudinal polarization with nearest-neighbor interactions, (b) longitudinal polarization with full-dipole interactions, (c) transverse polarization with nearest-neighbor interactions, and (d) transverse polarization with full-dipole interactions, in the η and κ planes. The black cross markers in (b) and (d) stand for the selected candidate data points to be examined in Figs. 8 and 9. The color code indicates the values of the quantity Δ .

behavior of κ as those shown in Fig. 4. Still, for the transverse NN case, some delocalized modes are no longer immune to disorder, and therefore these modes enter the localized stage when $\eta > 0.8$, the profile of which is consistent with what we studied in Fig. 5(b).

C. Phase diagrams

Finally, we present the complete results using a phase diagram by plotting the value of Δ in the η - κ grid of $[0, 0.9] \times [0, 1]$. The quantity η can help us segregate the three distinct phase regions. Figure 7 depicts the phase diagram of longitudinal and transverse eigenmodes with the two kinds of interactions in our quasiperiodic plasmonic model. We can identify and mark the three phases, i.e., the extended, localized, and intermediate phases in the phase diagrams according to Table I. It is discovered that in the limit of small κ the retarded plasmonic system reduces to the quasistatic model, which exhibits an ultrawide intermediate phase if the NN approximation is taken, while a finitely wide intermediate phase if adding the FD interactions as discussed above. Furthermore, moving away from this limit, it can be seen from Figs. 7(a)–7(d) that the edge between the localized phase and the intermediate phase is pushed toward larger η and then progressively repelled back with an increase in κ , especially for the transverse polarization shown in Figs. 7(c) and 7(d), suggesting that it is more difficult for the localized eigenmodes with transverse polarization to emerge in the frequency spectrum for a range of κ . In other words, for a range of η , the eigenmodes can be switched from intermediate to extended as κ increases, but further increasing κ can bring them back to intermediate states. Even though these features

also appear in the longitudinal eigenmodes, the control of retardation over them is less notable than the counterpart over transverse eigenmodes. As shown in Fig. 7(a), the phase edge of the longitudinal system in the NN case is pushed slightly only. However, in Fig. 7(b), the size of the intermediate phase is stretched for the range of κ between $0.32 < \kappa < 0.94$ as long as the FD interactions are introduced. In the meanwhile, for transverse polarization, the size of the intermediate phase with the NN cutoff shrinks for $\kappa > 0.26$ in Fig. 7(c), and a bright orange patch appears in the regions of strong disorder for $\kappa > 0.5$, which can be attributed to the localization of specific extended modes as discussed before [Fig. 5(b)]. Also, when considering the far-field interaction term, the intermediate phase with a finite width is quenched as κ goes larger, replaced by an ultrawide one instead as depicted in Fig. 7(d). Interestingly, we note that there is a bright orange spot in the vicinity of $\kappa \approx 0.5$ and $\eta \approx 0.18$ in this case, demonstrating an early appearance of the intermediate phase, which is distinct from the other scenarios. This is due to the zooming peaks in the scenario of transverse dipoles with full pair interactions as illustrated in Fig. 4(a).

To illuminate the role of retarded long-range interactions in mediating the phase boundary, we dwell into the complex eigenfrequency spectra in three different phases highlighted by the cross markers in Figs. 7(b) and 7(d) for both polarizations, which are displayed in Figs. 8(a)–8(c) and 9(a)–9(c). The pure Ohmic loss of $-\Gamma/2$ is marked by a dotted-dashed line, serving as a baseline to discern between guided and leaky modes. Furthermore, Figs. 8(d)–8(f) and 9(d)–9(f) showcase the respective dipole moment intensity $|p_v(n)|$ ($v = x, z$) along the sites n of the chain for longitudinal (x) and transverse polarizations (z) at three different filling indices, which are indicated by a circle, triangle, and square in Figs. 8(a)–8(c) and 9(a)–9(c), corresponding to different modes of interest within the spectra. Here, we focus on a 1000-nanoparticle chain perturbed by a moderate spacing disorder of $\eta = 0.5$, and discuss the unperturbed case in Appendix C. In a periodic 1D array of nanoparticles, the plasmonic modes can be classified either as leaky or not by the light-line condition since each mode has a well-defined Bloch wave vector. However, such a prescription is unsuitable for quasiperiodic systems due to the absence of translational symmetry. We can always consider the mode quality by examining the imaginary part of the eigenfrequency spectrum $\text{Im}(\omega)$, e.g., for the guided modes outside the light line, they are immune to the radiative losses, thereby possessing higher mode qualities than the leaky modes.

In longitudinal polarization, from the frequency spectra in Figs. 8(a)–8(c), we see three main clusters near the real frequencies of $0.998\omega_{\text{LSP}}$, ω_{LSP} , and $1.002\omega_{\text{LSP}}$ divided by the two fractal gaps at the fillings of β and $1 - \beta$ visible in gray-shaded blocks. At a weak retardation strength of $\kappa = 0.15$ shown in Fig. 8(a), the values of $\text{Im}(\omega)$ for the modes in the cluster near $1.002\omega_{\text{LSP}}$ ($l/N > \beta$) are larger than those in clusters near $0.998\omega_{\text{LSP}}$ ($l/N < 1 - \beta$) and ω_{LSP} ($1 - \beta < l/N < \beta$), and distributed in the vicinity of $-\Gamma/2$, which connotes that the modes with $l/N > \beta$ are of higher qualities and guided. As the retardation strength κ increases from 0.15 to 0.55 and subsequently to 0.95, the plasmonic system

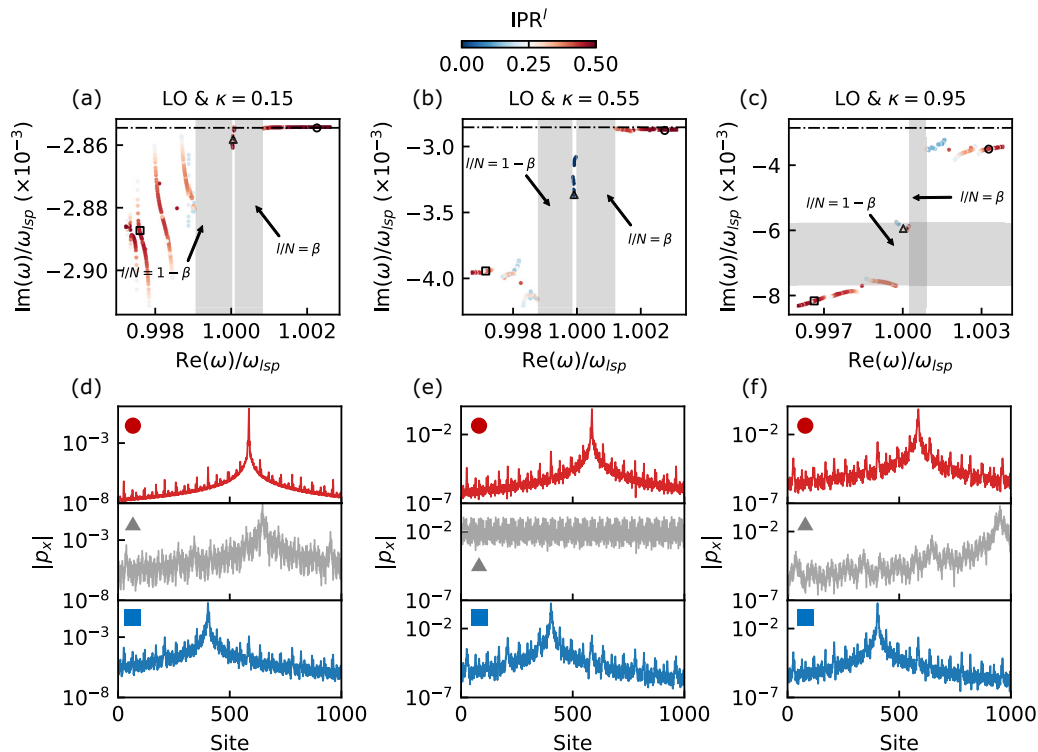


FIG. 8. Longitudinal eigenfrequency spectra of a finite $N = 1000$ plasmonic chain under a quasiperiodic disorder of $\eta = 0.5$ with different geometric configurations for (a) $\kappa = 0.15$, $a = 100$ nm, (b) $\kappa = 0.55$, $a = 360$ nm, and (c) $\kappa = 0.95$, $a = 630$ nm. These correspond to three typical phases with different retardation strengths for a fixed disorder considering the full-dipole interactions in Fig. 7(b). The two main spectral gaps with filling numbers $l/N = 1 - \beta$ and β are indicated by gray-shaded blocks. The dotted-dashed line portrays the Ohmic loss of $-\Gamma/2$. (d)–(f) Spatial decay profiles of three representative modes tagged by circle, triangle, and square markers at $l/N = 0.9$ (red), $l/N = 0.5$ (gray), and $l/N = 0.1$ (blue) from the top to bottom rows.

undergoes a localized-intermediate-localized phase transition. The modes with $l/N > \beta$ go from being guided and weakly leaky in Figs. 8(a) and 8(b) to attaining a fully leaky nature in Fig. 8(c). In parallel, the modes with $l/N < \beta$ display an enhanced radiating behavior.

For these guided modes, just as quasistatic plasmons, they can be subject to Anderson localization and well localized at certain sites with very high IPRs, which is exemplified in the top row of Fig. 8(d) by the spatial distribution of dipoles with $l/N = 0.9$. The intensity of dipole moments is strongly concentrated on the localization center, and drops steeply to small value with an exponential decay, crossing over to a power-law tail from the near-field term decaying as $1/x^3$. In the same vein, for the cases of weakly leaky modes, they can also exhibit both exponential and power-law decaying behaviors, as shown in the middle and bottom rows of Fig. 8(d) and in the top row of Fig. 8(e), despite radiating a little energy into the photonic background. We note that the same mechanism occurs for leaky modes with $l/N < 1 - \beta$, which are highly radiating and dominated by $1/x^2$ intermediate-field interactions. These modes can still manifest a localization behavior with a slower power-law decay as the case of $l/N = 0.1$ shown in the bottom row of Figs. 8(e) and 8(f). Interestingly, at the retardation of $\kappa = 0.55$, the modes with $1 - \beta < l/N < \beta$ that leak out less reveal a very low IPR and are extended over the chain as suggested by the dipole distribution of $l/N = 0.5$ in the middle row of Fig. 8(e), which boils down to the coupling with a retarded free-space radiation. The interference

effect from this radiation delocalizes the spatial localization properties of these leaky modes, allowing the emergence of the intermediate phase in Fig. 7(b). By further amplifying the retardation strength to $\kappa = 0.95$ in the middle row of panel 8(f), the modes come back to the localized state again, therefore the plasmonic system acquires a localized phase in the leaky sense.

Next, we take a look at transverse polarization, which shares the same spectral structure with that of longitudinal polarization at the weak retardation of $\kappa = 0.05$, except for a reverse order with respect to the real frequency $\text{Re}(\omega)$ as shown in Fig. 9(a). We can also obtain a cluster of guided modes in proximity to $0.999\omega_{\text{LSP}}$, corresponding to the filling numbers of $l/N > \beta$. Additionally, two clusters of weakly leaky modes manifest themselves in the vicinity of ω_{LSP} with $1 - \beta < l/N < \beta$ and $1.001\omega_{\text{LSP}}$ with $l/N > \beta$. As we further elevate the retardation tuning parameter, in the cases of $\kappa = 0.45$ and 0.75 presented in Figs. 9(b) and 9(c), these transversely polarized modes become more radiating progressively as the longitudinal polarization, but we cannot delineate them on the basis of filling numbers. This arises from the retarded long-range interaction, which can close the *in situ* spectral gaps, accordingly, disrupting the hierarchy of fractal gaps. For example, the one located at $l/N = \beta$ is closed as indicated by the dotted vertical line in Figs. 9(b) and 9(c). Likewise, this long-range interaction can destroy the *in situ* localization hierarchy, that is, the mobility edge, as discussed in Fig. 5(c).

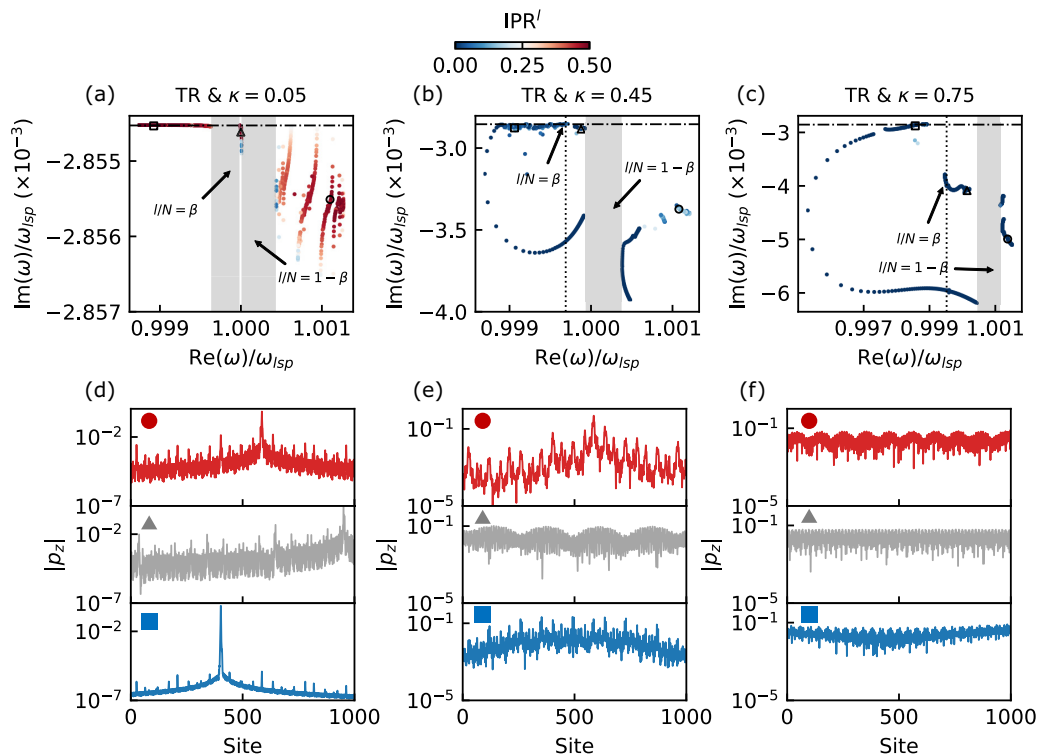


FIG. 9. Transverse eigenfrequency spectra of a finite $N = 1000$ plasmonic chain under a quasiperiodic disorder of $\eta = 0.5$ with different geometric configurations for (a) $\kappa = 0.05$, $a = 33$ nm, (b) $\kappa = 0.45$, $a = 300$ nm, and (c) $\kappa = 0.75$, $a = 500$ nm. These also correspond to three typical phases with different retardation strengths for a fixed disorder considering the full-dipole interactions on the cross markers in Fig. 7(b). The two main spectral gaps with filling numbers $l/N = 1 - \beta$ and $l/N = \beta$ as well as the Ohmic loss of $-\Gamma/2$ are indicated in the same way as Fig. 8. (d)–(f) Spatial decay profiles of three representative modes labeled by circle, triangle, and square markers at $l/N = 0.1$ (red), $l/N = 0.5$ (gray), and $l/N = 0.9$ (blue) from the top to bottom rows.

In Fig. 9(d), at the given retardation strength of $\kappa = 0.05$, we show the decay profile of the transverse dipole eigenmodes with $l/N = 0.1, 0.5$, and 0.9 ranging from the top to bottom rows, respectively. It is found that these guided or weakly leaky modes can be localized by a quasiperiodic disorder, representing algebraic tails with longer decay lengths than the longitudinal counterpart in addition to the exponential peaks. Therefore, this case, free of the dictation of far-field interactions, can present high IPRs and a localized phase. In Figs. 9(e) and 9(f), we display the same quantities for the transverse dipoles with the same fillings at $\kappa = 0.45$ and 0.75 , which are located in the intermediate and extended phases individually. We can see that the domination of slowly decaying long-range interactions from the well coupling with photons on the collective dipoles allows them to inherit the robustness against localization, which causes them to be spatially delocalized over the chain even for those modes with a few radiative losses, as shown in the middle row of Fig. 9(e) and the bottom rows of Figs. 9(e) and 9(f). Nevertheless, from the upper row of Fig. 9(e), we note that a fully leaky mode of $l/N = 0.9$ with a slightly high IPR is confined to multiple nonadjacent sites followed by high-amplitude algebraic tails, which is commonly referred to a semilocalized polaritonic mode as studied in Refs. [96,97]. These semilocalized modes can be regarded as spatially localized modes, characterized by an exponential peak exhibiting a size-independent IPR, accompanied by long-range tails that have undergone significant amplification to attain comparable magnitudes with the

central peak. In a nutshell, it can be confirmed by the above mode-dependent decay behaviors that there is no specific law between mode quality and spatial localization for both polarizations. More precisely, these longitudinally or transversely polarized plasmonic dipoles can be localized in a highly or lowly leaky sense, which was also discussed in a 2D 12-fold quasicrystalline plasmonic lattice [81].

In electronic systems, non-Hermiticity can compete with the Anderson localization and lead to delocalization of bulk states, and also enables a localization at edges due to the non-Hermitian skin effect [98–100]. Very recently, it has been argued that there is a duality between non-Hermitian Hamiltonians in flat spaces and their Hermitian counterparts in curved spaces [101], which means that nonlinearity can serve as an equivalent route toward non-Hermiticity. Meanwhile, the generation of moving localized modes has been observed in the nonlinear plasmonic arrays [102–104], therefore, we expect a connection between non-Hermiticity and localization transitions presented in the phase diagrams. To corroborate that the localization transitions are tied to non-Hermiticity induced by retardation, we measure the difference between the right and left eigenmodes ($|\mathbf{p}_R^l\rangle$ and $|\mathbf{p}_L^l\rangle$) of the eigenvalue l in the finite plasmonic chain through the phase rigidity defined as [105]

$$r_p^l = \frac{|\langle \mathbf{p}_R^l | \mathbf{p}_L^l \rangle|}{\sqrt{\langle \mathbf{p}_R^l | \mathbf{p}_R^l \rangle \langle \mathbf{p}_L^l | \mathbf{p}_L^l \rangle}} \quad (16)$$

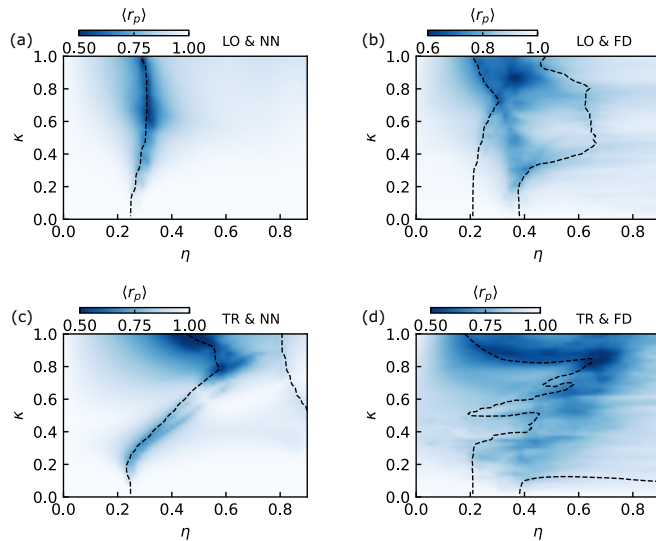


FIG. 10. The mean phase rigidity $\langle r_p \rangle$ of plasmonic eigenmodes in the η - κ space for four distinct cases of polarization and interaction schemes. These cases include (a) longitudinal polarization with nearest-neighbor interactions, (b) longitudinal polarization with full-dipole interactions, (c) transverse polarization with nearest-neighbor interactions, and (d) transverse polarization with full-dipole interactions. The black dashed lines mark the boundaries between the three localization phases: extended, intermediate, and localized, which are determined by the differential quantity $|\partial\Delta/\partial\eta|$.

with $0 \leq r_p^l \leq 1$. For Hermitian systems, rigidity is exactly 1 for all eigenmodes, while for non-Hermitian systems where $|\mathbf{p}_L^l| \neq |\mathbf{p}_R^l|$, we generally have $r_p^l < 1$, and near the exceptional points, it approaches 0. Therefore, phase rigidity can be regarded as an indicator of the strength of non-Hermiticity. Also, we can define the mean phase rigidity of all N eigenmodes as

$$\langle r_p \rangle = \frac{\sum_{l=1}^N r_p^l}{N}. \quad (17)$$

In Fig. 10, we show $\langle r_p \rangle$ as functions of η and κ for transverse and longitudinal polarizations under different interactions. Notably, the bright grooves formed by the comparatively low $\langle r_p \rangle$ values show a nonmonotonic dependence on κ , which may be attributed to the competition between the localization effect induced by the disorder and the non-Hermitian retarded effect.

We also present the boundaries among the extended, intermediate, and localized phases in Fig. 10, which are derived from computing the maximum $|\partial\Delta/\partial\eta|$. In all the cases investigated in this study, we find that $\langle r_p \rangle$ shows lower values along the phase boundaries, which means that the critical regions possess strong non-Hermiticity. In addition, we find that the FD interactions strengthen the diffusion of non-Hermiticity, hence resulting in ambiguous phase boundaries observed from $\langle r_p \rangle$ in Figs. 10(b) and 10(d) and complicated boundaries of phase transitions in Figs. 7(b) and 7(d). At last, we stress that although the phase edge in the upper right corner of Fig. 10(c) is determined due to relatively high values of $|\partial\Delta/\partial\eta|$, there are still some modes that remain extended beyond this edge, indicating that the plasmonic system is still

in the intermediate phase. This is confirmed by the weaker non-Hermiticity suggested by higher $\langle r_p \rangle$ values. Therefore, caution should be exercised when interpreting the phase transition based solely on the derived quantity $|\partial\Delta/\partial\eta|$, and other indicators should also be considered.

Before summarizing, we would like to make some remarks on the choice of particle size a in plasmonic chains. Specifically, we require small particle sizes to ensure that polarizability with and without radiative correction yields similar results, although radiative correction allows for larger particles. We choose a radius that is large enough for classical treatment but small enough to linearize the dyadic Green's function. Qualitatively similar results are expected for larger particles, although radiative effects would be more prominent. This is because differences in particle size influence only the fidelity and frequency spectrum profiles of modes, without impacting their spatial localization within the framework of linearized Green's functions. Aside from that, there is a trade-off between particle radius a and minimum spacing d_{\min} . Due to the dipole approximation constraint, calculations are limited to spacings d that satisfy $d_{\min} = \min_n(x_{n+1} - x_n) > 3a$. However, larger a and d are experimentally favorable since the difficulty of fabrication, and an optimal pair of a and d , should be selected to observe the intermediate phase and mobility edge in the plasmonic chains.

Regarding the experimental implementation of our model, which has irrational-number interparticle spacings, we provide a quantitative estimation of the effective region for our plasmonic AAH model as follows. Taking into account a rational truncation of the irrational $\beta = (\sqrt{5} - 1)/2$, which is denoted as $T_n(\beta) = \frac{\lceil 10^n \beta \rceil}{10^n}$ with n being the remaining decimal places and $\lceil \cdot \rceil$ being the ceiling function. From the spatial distribution of the dipole moment amplitudes for the longitudinal modes with $N = 1000$, $\eta = 0.5$, and $\kappa = 0.5$, it turns out that the Anderson localization persists when the truncation is $n \geq 4$. This result means that a position precision of 4 decimal digits is enough for experimental observations of a finite chain with 1000 nanoparticles.

IV. CONCLUSION

In this work, we used the coupled dipole method to investigate localization properties including the localization transition, mobility edge, and intermediate phases in 1D quasiperiodic plasmonic chains. We introduced a quasiperiodic order by incommensurate modulations on the distances between adjacent InSb nanoparticles in the chains, leading to a mimicry of the off-diagonal AAH model. Through analysis of IPR, NPR, frequency spectrum, and spatial distribution of eigenmodes, we observed the mobility edge and intermediate phase in the quasistatic model with long-range dipole interactions. We also examined the intermediate phase in the case of nearest-neighbor approximation, which features an ultrabroad width.

Subsequently, we explored the impact of non-Hermiticity on the localization properties of quasidisordered plasmonic chains by including the effect of retardation and employing the linearized Green's function. We described in detail how the localization properties of the retarded system depend on the retardation tuning parameter κ and the modulation

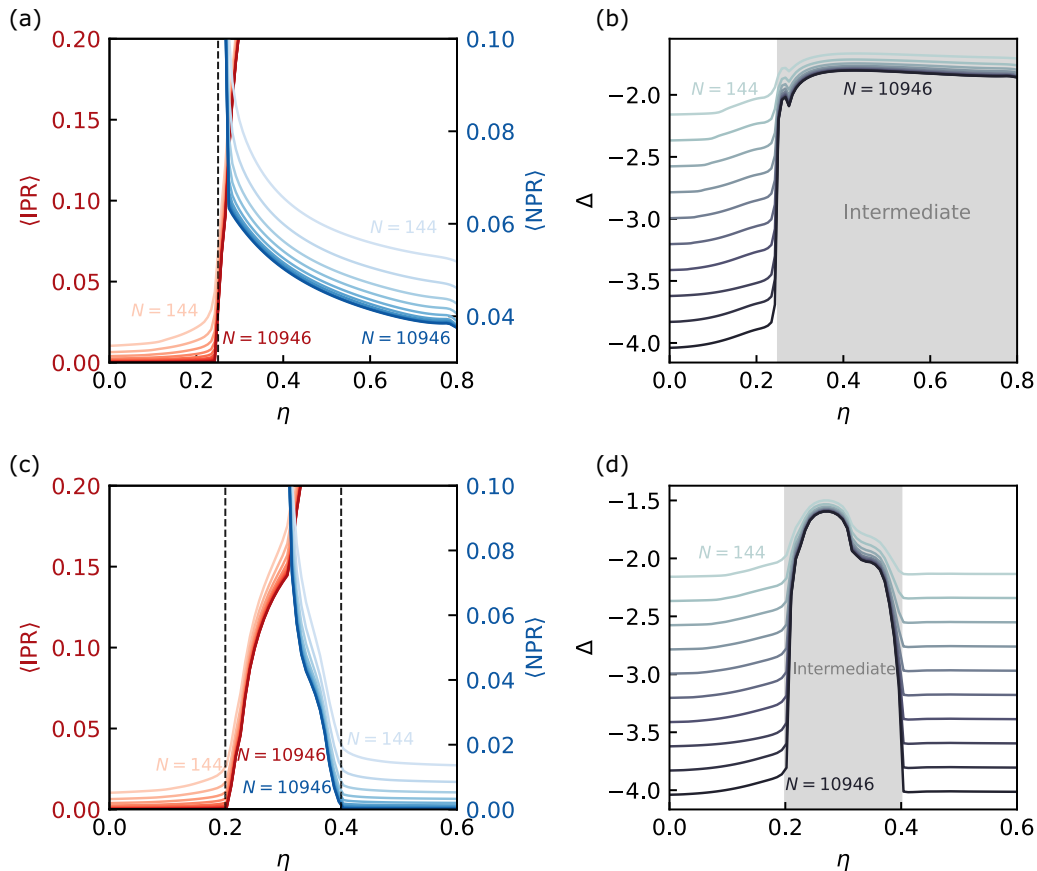


FIG. 11. The mean inverse partition ratio ($\langle \text{IPR} \rangle$), mean normalized partition ratio ($\langle \text{NPR} \rangle$), and quantity Δ of transverse eigenmodes as a function of η for different system sizes N ranging from 144 to 10946 in the Fibonacci order (light to deep color). Here, the nearest-neighbor (NN) and full-dipole (FD) interactions are considered. The critical point of the phase transition and the intermediate phase are marked by a black-dashed line and a gray-shaded block, separately. (a), (b) $\langle \text{IPR} \rangle$, $\langle \text{NPR} \rangle$, and Δ with NN interactions. (c), (d) The same quantities with FD interactions.

amplitude η , and mapped out the localization phase diagram as a function of these parameters. In the retarded regime, we found that significant differences emerge for diverse polarizations and interactions, originating from the different decay terms in Green's functions. We observed that for longitudinal polarization, Anderson localization is slightly affected, and the extremely wide intermediate phase region remains unchanged with nearest-neighbor interactions. However, the presence of long-range interactions broadens the initially narrow intermediate phase region for a range of κ . In contrast, in the case of transverse polarization, the phase transition undergoes a significant change even under nearest-neighbor interactions, causing the extremely wide intermediate phase to contract within a specific κ range. Once long-range interactions are taken into account, the previously intermediate phase with a finite width disappears and is replaced by an extremely wide intermediate phase. We also elaborated the role of retarded long-range interactions in mediating localization phases by showcasing mode qualities and decay profiles in distinct phases. For mode quality and localization profile, there is no specific law between them, that is, plasmonic modes could be localized in a highly or lowly leaky state for both polarizations.

Finally, we established a connection between non-Hermiticity and phase transition by the mean phase rigidity

$\langle r_p \rangle$, which revealed that strong non-Hermiticity is built along the phase boundary. We also anticipate that similar localization behavior could be observed in other dipolar systems, such as phonon polaritons in SiC nanoparticle chains and cold-atom chains, due to the same type of hoppings. This work extends the concept of mobility edge and intermediate phase to plasmonic systems and paves the way for further exploration of the physics of Anderson localization on plasmonic platforms.

ACKNOWLEDGMENT

We gratefully acknowledge financial support from the National Natural Science Foundation of China (Grant No. 12074091) and the Shenzhen Science and Technology Program (Grant No. RYX20221008092848063).

APPENDIX A: FINITE-SIZE EFFECT

To ensure that the ultrawide intermediate phase observed in Fig. 2(a) for the NN case is independent of finite-size effect, we perform additional calculations on the $\langle \text{IPR} \rangle$, $\langle \text{NPR} \rangle$, and Δ in this case for different system sizes corresponding to Fibonacci numbers F_n from 144 to 10946 ($N \in \{F_n | 12 \leq n \leq 21, n \in \mathbb{Z}^+\}$), as shown in Fig. 11. The black dashed line and the

gray-shaded region represent the critical point of the phase transition and the intermediate phase, respectively. In the NN case depicted in Figs. 11(a) and 11(b), as the system size N increases, it is evident that $\langle \text{IPR} \rangle$ decreases and approaches zero when $\eta < \eta_c \approx 0.25$, while $\langle \text{NPR} \rangle$ remains finite when $\eta > \eta_c \approx 0.25$, yielding a stable intermediate phase region that is guaranteed by Δ convergent to the interval of $[-2, -1.5]$. This indicates that the ultrawide intermediate phase observed in the NN case is not a finite-size effect, which may be caused by extended modes near the localized surface plasmon resonant frequency ω_{LSP} . These modes align with the Dyson singularity in the density of states of the 1D NN tight-binding model with the off-diagonal disorder [106,107]. Rather, with the FD interactions included, $\langle \text{IPR} \rangle$ and $\langle \text{NPR} \rangle$ approach zero rapidly in the delocalized ($\eta < \eta_{c1} \approx 0.2$) and localized phases $\eta > \eta_{c2} \approx 0.4$ as N increases [Fig. 11(c)], leading to an intermediate phase with a narrow width [Fig. 11(d)].

APPENDIX B: MOBILITY EDGES IN THE QUASISTATIC REGIME

In the quasistatic regime, we can derive an analytical solution for the mobility edges for the nearest-neighbor case using the energy match model [108]. The basic idea of this model involves approximating quasiperiodic disordered models utilizing an ensemble of ordered models $\{H_\alpha\}$. Under the nearest-neighbor approximation, the effective tight-binding Hamiltonian of these models, labeled by $\alpha \in \{1, 2, \dots, N\}$, is constructed from the near-field Green's matrix, which reads as

$$H_\alpha = - \sum_{n=1}^{N-1} t_\alpha (|p_n\rangle\langle p_{n+1}| + |p_{n+1}\rangle\langle p_n|), \quad (\text{B1})$$

where $t_\alpha = \frac{f_v}{[1+\eta \cos(2\pi\beta\alpha+\phi)]^3}$ is the hopping amplitude between two adjacent sites, and the polarization-dependent factor $f_x = -\frac{1}{2\pi}$ (f_y or $f_z = \frac{1}{4\pi}$) for the longitudinal (transverse) modes arises from the anisotropy of the dipolar interaction. The exact diagonalization of a Toeplitz tridiagonal matrix H_α in the presence of a constant t_α permits the following eigenvalue spectrum:

$$E_\alpha^l = -2t_\alpha \cos \frac{\pi l}{N+1}, \quad l \in \{1, 2, \dots, N\}. \quad (\text{B2})$$

Obviously, the extended phase region for the model H_α belongs to the spectrum interval

$$E_\alpha \in (-2t_\alpha, 2t_\alpha). \quad (\text{B3})$$

Note that if a given energy E is ergodic and falls within the energy spectra of all the models H_α , we expect the corresponding eigenstate to be extended. Therefore, the energy domain of the extended states will be the intersection of the energy spectrum sets E_α as

$$E \in \bigcap_{\alpha=1}^N E_\alpha, \quad \in \left(-\frac{2f_v}{(1+\eta)^3}, \frac{2f_v}{(1+\eta)^3} \right). \quad (\text{B4})$$

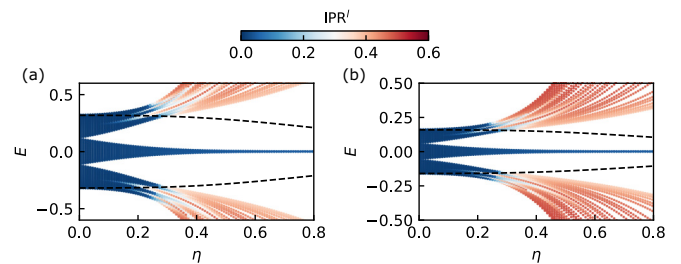


FIG. 12. The quasistatic eigenvalue spectra of an $N = 100$ nanoparticle chain as a function of η for (a) longitudinal and (b) transverse polarizations under the nearest-neighbor approximation. The colors represent the IPR of each eigenmode, and the black dashed curves mark the solved mobility edges.

It is easy to see that the respective energy domains of the extended phase for longitudinal and transverse polarizations are

$$E \in \begin{cases} \left(-\frac{1}{\pi(1+\eta)^3}, \frac{1}{\pi(1+\eta)^3} \right), & \nu = x \\ \left(-\frac{1}{2\pi(1+\eta)^3}, \frac{1}{2\pi(1+\eta)^3} \right), & \nu = y, z. \end{cases} \quad (\text{B5})$$

The upper bound and lower bounds define two mobility edges as the disorder parameter η varies, which serve as boundaries that separate extended states from localized states.

To verify the above mobility edges, we plot the eigenvalues of longitudinal and transverse modes with increasing disorder amplitude η in Fig. 12. The color of each point encodes the IPR value of the eigenmodes. We observe that the boundary of the blue region roughly corresponds to the mobility edges determined by the energy matching method.

APPENDIX C: EFFECTS OF QUASIPERIODIC DISORDER ON BAND STRUCTURES

To delve into the effect of quasiperiodic disorder on the plasmonic band structure, we first calculate the eigenpairs of an equidistant chain consisting of $N = 1000$ nanoparticles via the linearized Green's function method for comparison, and the real and imaginary parts of eigenfrequencies are shown in Figs. 13(a) and 13(b) for the longitudinal and transverse modes. The dispersion relation depicted by the blue dots in Figs. 13(a) and 13(b) is obtained by sorting the eigenmodes in ascending order of the mode index l , which is equal to the node number of $\text{Re}(p)$ plus 1, and the Bloch wave vector q is given by

$$qd/\pi = \frac{(N-2)l+1}{N(N-1)}, \quad (\text{C1})$$

where l is the mode index and N is the number of nanoparticles in the chain. The results are in agreement with the previous arguments of renormalized dispersion curves for the 1D regular plasmonic arrays [78,109,110]. We observe that at $q = 0$, the longitudinal mode reaches a minimum lying below ω_{LSP} , while the transverse mode demonstrates a maximum, positioned above ω_{LSP} , which implies the opposite signs of near-field pair dipole interactions for these two modes. We also see that the light line $k = \text{Re}(\omega)/c$ marked by the gray dashed-dotted line divides the eigenmodes into two parts,

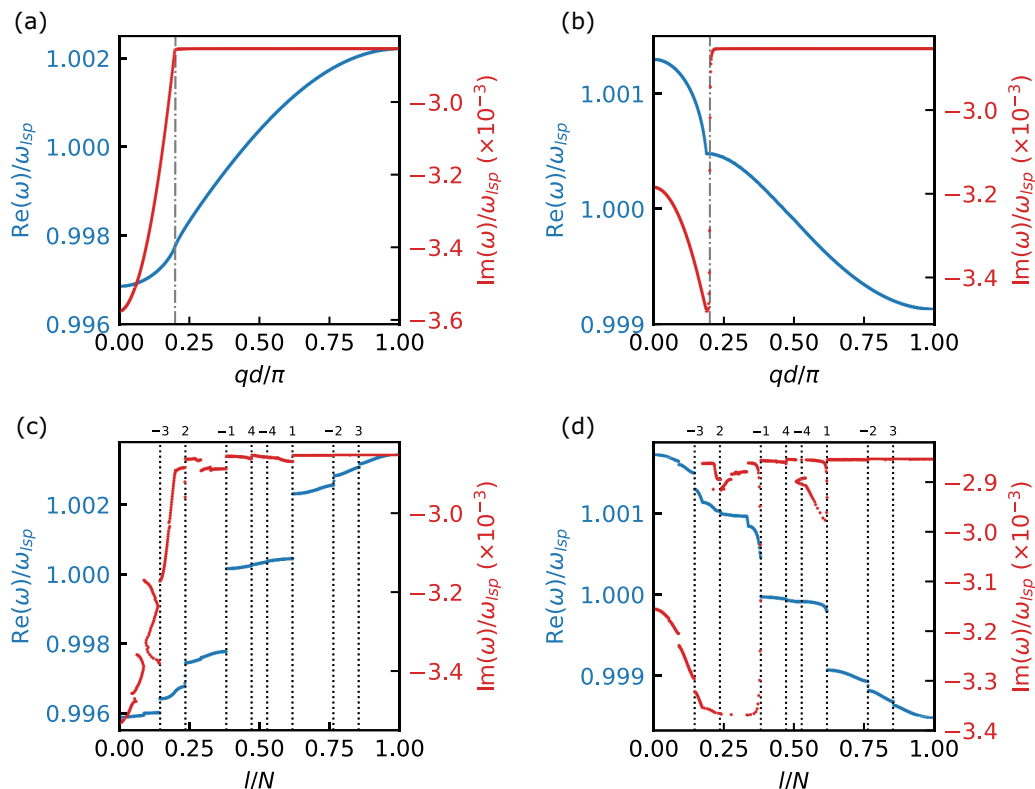


FIG. 13. (a), (b) Real (blue dots) and imaginary (red dots) parts of the dispersion relation of regular plasmonic chains ($\eta = 0$) for the longitudinal and transverse modes. The dispersion of light in free space (gray dashed-dotted line) is also shown. (c), (d) The frequency spectrum of quasiperiodic plasmonic chains ($\eta = 0.3$) with topological numbers of spectral gaps being labeled by dotted lines for longitudinal and transverse modes. The results are calculated on parameters of $\kappa = 0.2$ ($d = 1.08 \mu\text{m}$), $a = 200 \text{ nm}$, and $N = 1000$.

leaky (radiating) modes and guided (nonradiating) modes. Within the light line ($q < k$), leaky modes with large negative values of $\text{Im}(\omega)$ suffer from both Ohmic and radiative losses. In contrast, the guided modes above the light line ($q > k$) are free of radiative damping and possess the Ohmic loss only. It should be noted that the anticrossing between the dispersion curve and the light line is only observed for the transverse modes in Fig. 13(b), signaling a strong polaritonic mixing between plasmons and photons, which is attributed to the transversality of light waves, and hence they can couple well to transverse plasmons. This intense coupling also yields a step discontinuity at the anticrossing point for the imaginary part, and a long-range far-field interaction term in the full Green's function for the transverse polarization. For the longitudinal case in Fig. 13(a), although there is no such cusp in the associated dispersion and no discontinuity in the imaginary counterpart, a hybridization between collective plasmons and the photonic environment is still present in the form of radiative loss [90,111].

For a quasiperiodic chain with a spacing disorder of $\eta = 0.3$, we plot the eigenfrequency spectra as a function of the filling number l/N for the longitudinal and transverse modes in Figs. 13(c) and 13(d). In both polarizations, we see that the spectra are separated by fractal gaps appearing

at fillings of $\{[3(1 - \beta)], [2\beta], 1 - \beta, \beta, [4\beta], [4(1 - \beta)], 2(1 - \beta), [3\beta]\}$ with $\{\cdot\}$ being the fractional part of a number. These gaps can be denoted briefly as their topological indices $[-3, 2, -1, 4, -4, 1, -2, 3]$, which are protected by gap labeling theorem [112], and they are portrayed by black dotted lines in Figs. 13(c) and 13(d). The two main gaps that establish the largest gap width are located at the fillings $1 - \beta$ or β , and the other six minigaps with smaller gap widths are classified as $\{2\beta\}, 2(1 - \beta)$, etc. In principle, for an irrational number of β , irrespective of the quasiperiodic strength η , the filling sequence will exhibit an infinite number of gaps in the thermodynamic limit. These gaps separate the unperturbed band into a series of subbands, which present different localization transitions at different disorder amplitudes η as reported in the main text. We can still adopt the radiative loss to classify these modes into leaky and guided parts, even though there is no Bloch wave vector for the disordered structure. From the imaginary spectra, it is observed that destruction of periodicity can give rise to additional scattering losses for guided modes in subbands above the real frequency of $0.9975\omega_{\text{LSP}}$ for longitudinal modes or below the real frequency of $1.0005\omega_{\text{LSP}}$ for transverse modes, whereas it can also suppress the losses for the leaky modes, leading to an overall increase in the values of $\text{Im}(\omega)$ [78,113].

- [1] A. Lagendijk, B. Van Tiggelen, and D. S. Wiersma, Fifty years of Anderson localization, *Phys. Today* **62**(8), 24 (2009).
- [2] P. A. Lee and D. S. Fisher, Anderson localization in two dimensions, *Phys. Rev. Lett.* **47**, 882 (1981).
- [3] P. W. Anderson, D. J. Thouless, E. Abrahams, and D. S. Fisher, New method for a scaling theory of localization, *Phys. Rev. B* **22**, 3519 (1980).
- [4] N. Mott, The mobility edge since 1967, *J. Phys. C: Solid State Phys.* **20**, 3075 (1987).
- [5] G. Semeghini, M. Landini, P. Castilho, S. Roy, G. Spagnolli, A. Trenkwalder, M. Fattori, M. Inguscio, and G. Modugno, Measurement of the mobility edge for 3d Anderson localization, *Nat. Phys.* **11**, 554 (2015).
- [6] J.-B. Suck, M. Schreiber, and P. Häussler, *Quasicrystals: An Introduction to Structure, Physical Properties and Applications*, Vol. 55 (Springer, New York, 2013).
- [7] V. Goblot, A. Štrkalj, N. Pernet, J. L. Lado, C. Dorow, A. Lemaître, L. Le Gratiet, A. Harouri, I. Sagnes, S. Ravets *et al.*, Emergence of criticality through a cascade of delocalization transitions in quasiperiodic chains, *Nat. Phys.* **16**, 832 (2020).
- [8] C. Wang, T. Cheng, Z. Liu, F. Liu, and H. Huang, Structural amorphization-induced topological order, *Phys. Rev. Lett.* **128**, 056401 (2022).
- [9] H. Wang, X. Zheng, J. Chen, L. Xiao, S. Jia, and L. Zhang, Fate of the reentrant localization phenomenon in the one-dimensional dimerized quasiperiodic chain with long-range hopping, *Phys. Rev. B* **107**, 075128 (2023).
- [10] S. Aubry and G. André, Analyticity breaking and Anderson localization in incommensurate lattices, *Ann. Isr. Phys. Soc.* **3**, 133 (1980).
- [11] M. Kohmoto, L. P. Kadanoff, and C. Tang, Localization problem in one dimension: Mapping and escape, *Phys. Rev. Lett.* **50**, 1870 (1983).
- [12] S. Ostlund, R. Pandit, D. Rand, H. J. Schellnhuber, and E. D. Siggia, One-dimensional Schrödinger equation with an almost periodic potential, *Phys. Rev. Lett.* **50**, 1873 (1983).
- [13] S. Y. Jitomirskaya, Metal-insulator transition for the almost mathieu operator, *Ann. Math.* **150**, 1159 (1999).
- [14] J. Biddle and S. Das Sarma, Predicted mobility edges in one-dimensional incommensurate optical lattices: An exactly solvable model of Anderson localization, *Phys. Rev. Lett.* **104**, 070601 (2010).
- [15] S. Ganeshan, J. H. Pixley, and S. Das Sarma, Nearest neighbor tight binding models with an exact mobility edge in one dimension, *Phys. Rev. Lett.* **114**, 146601 (2015).
- [16] J. Biddle, B. Wang, D. J. Priour Jr, and S. Das Sarma, Localization in one-dimensional incommensurate lattices beyond the Aubry-André model, *Phys. Rev. A* **80**, 021603(R) (2009).
- [17] J. Biddle, D. J. Priour Jr, B. Wang, and S. Das Sarma, Localization in one-dimensional lattices with non-nearest-neighbor hopping: Generalized Anderson and Aubry-André models, *Phys. Rev. B* **83**, 075105 (2011).
- [18] D. Vu and S. D. Sarma, Generic mobility edges in several classes of duality-breaking one-dimensional quasiperiodic potentials, *Phys. Rev. B* **107**, 224206 (2023).
- [19] S. Das Sarma, S. He, and X. C. Xie, Mobility edge in a model one-dimensional potential, *Phys. Rev. Lett.* **61**, 2144 (1988).
- [20] S. Das Sarma, S. He, and X. C. Xie, Localization, mobility edges, and metal-insulator transition in a class of one-dimensional slowly varying deterministic potentials, *Phys. Rev. B* **41**, 5544 (1990).
- [21] X. Li, X. Li, and S. Das Sarma, Mobility edges in one-dimensional bichromatic incommensurate potentials, *Phys. Rev. B* **96**, 085119 (2017).
- [22] X. Li and S. Das Sarma, Mobility edge and intermediate phase in one-dimensional incommensurate lattice potentials, *Phys. Rev. B* **101**, 064203 (2020).
- [23] H. P. Lüschen, S. Scherg, T. Kohlert, M. Schreiber, P. Bordia, X. Li, S. Das Sarma, and I. Bloch, Single-particle mobility edge in a one-dimensional quasiperiodic optical lattice, *Phys. Rev. Lett.* **120**, 160404 (2018).
- [24] Y. Wang, X. Xia, L. Zhang, H. Yao, S. Chen, J. You, Q. Zhou, and X.-J. Liu, One-dimensional quasiperiodic mosaic lattice with exact mobility edges, *Phys. Rev. Lett.* **125**, 196604 (2020).
- [25] H. Jiang, L.-J. Lang, C. Yang, S.-L. Zhu, and S. Chen, Interplay of non-Hermitian skin effects and Anderson localization in nonreciprocal quasiperiodic lattices, *Phys. Rev. B* **100**, 054301 (2019).
- [26] Y. Liu, X.-P. Jiang, J. Cao, and S. Chen, Non-Hermitian mobility edges in one-dimensional quasicrystals with parity-time symmetry, *Phys. Rev. B* **101**, 174205 (2020).
- [27] Y. Liu, Y. Wang, Z. Zheng, and S. Chen, Exact non-Hermitian mobility edges in one-dimensional quasicrystal lattice with exponentially decaying hopping and its dual lattice, *Phys. Rev. B* **103**, 134208 (2021).
- [28] X. Xia, K. Huang, S. Wang, and X. Li, Exact mobility edges in the non-Hermitian t_1 - t_2 model: Theory and possible experimental realizations, *Phys. Rev. B* **105**, 014207 (2022).
- [29] S. Longhi, Phase transitions in a non-Hermitian Aubry-André-Harper model, *Phys. Rev. B* **103**, 054203 (2021).
- [30] C. Wu, J. Fan, G. Chen, and S. Jia, Non-hermiticity-induced reentrant localization in a quasiperiodic lattice, *New J. Phys.* **23**, 123048 (2021).
- [31] B. Zhu, L.-J. Lang, Q. Wang, Q. J. Wang, and Y. D. Chong, Topological transitions with an imaginary Aubry-André-Harper potential, *Phys. Rev. Res.* **5**, 023044 (2023).
- [32] C. Gross and I. Bloch, Quantum simulations with ultracold atoms in optical lattices, *Science* **357**, 995 (2017).
- [33] N. R. Cooper, J. Dalibard, and I. B. Spielman, Topological bands for ultracold atoms, *Rev. Mod. Phys.* **91**, 015005 (2019).
- [34] H. Zhai, *Ultracold Atomic Physics* (Cambridge University Press, Cambridge, 2021).
- [35] D. J. Boers, B. Goedeke, D. Hinrichs, and M. Holthaus, Mobility edges in bichromatic optical lattices, *Phys. Rev. A* **75**, 063404 (2007).
- [36] F. A. An, E. J. Meier, and B. Gadway, Engineering a flux-dependent mobility edge in disordered zigzag chains, *Phys. Rev. X* **8**, 031045 (2018).
- [37] F. A. An, K. Padavić, E. J. Meier, S. Hegde, S. Ganeshan, J. H. Pixley, S. Vishveshwara, and B. Gadway, Interactions and mobility edges: Observing the generalized Aubry-André model, *Phys. Rev. Lett.* **126**, 040603 (2021).
- [38] A. Marie, D. P. Kooi, J. Grossi, M. Seidl, Z. H. Musslimani, K. J. H. Giesbertz, and P. Gori-Giorgi, Real-space Mott-Anderson electron localization with long-range interactions, *Phys. Rev. Res.* **4**, 043192 (2022).
- [39] F. Evers and A. D. Mirlin, Anderson transitions, *Rev. Mod. Phys.* **80**, 1355 (2008).

- [40] G. Li, F. Xu, and J. Wang, Universal behaviors of magnon-mediated spin transport in disordered nonmagnetic metal-ferromagnetic insulator heterostructures, *Front. Phys.* **18**, 33310 (2023).
- [41] P. Wang, Y. Zheng, X. Chen, C. Huang, Y. V. Kartashov, L. Torner, V. V. Konotop, and F. Ye, Localization and delocalization of light in photonic moiré lattices, *Nature (London)* **577**, 42 (2020).
- [42] F. Riboli, N. Caselli, S. Vignolini, F. Intonti, K. Vynck, P. Barthelemy, A. Gerardino, L. Balet, L. H. Li, A. Fiore *et al.*, Engineering of light confinement in strongly scattering disordered media, *Nat. Mater.* **13**, 720 (2014).
- [43] A. Chabanov, M. Stoytchev, and A. Genack, Statistical signatures of photon localization, *Nature (London)* **404**, 850 (2000).
- [44] H. Hu, A. Strybulevych, J. Page, S. E. Skipetrov, and B. A. van Tiggelen, Localization of ultrasound in a three-dimensional elastic network, *Nat. Phys.* **4**, 945 (2008).
- [45] D. T. Smith, C. P. Lorenson, R. B. Hallock, K. R. McCall, and R. A. Guyer, Third sound on substrates patterned with periodic and random disorder: Evidence for classical wave localization, *Phys. Rev. Lett.* **61**, 1286 (1988).
- [46] S. He and J. D. Maynard, Detailed measurements of inelastic scattering in Anderson localization, *Phys. Rev. Lett.* **57**, 3171 (1986).
- [47] W.-B. Shi, L.-Z. Liu, R. Peng, D.-H. Xu, K. Zhang, H. Jing, R.-H. Fan, X.-R. Huang, Q.-J. Wang, and M. Wang, Strong localization of surface plasmon polaritons with engineered disorder, *Nano Lett.* **18**, 1896 (2018).
- [48] S. A. Maier, *Plasmonics: Fundamentals and Applications*, Vol. 1 (Springer, Berlin, 2007).
- [49] M. L. Brongersma and P. G. Kik, *Surface Plasmon Nanophotonics*, Vol. 131 (Springer, Dordrecht, 2007).
- [50] J. Zhang, L. Zhang, and W. Xu, Surface plasmon polaritons: Physics and applications, *J. Phys. D: Appl. Phys.* **45**, 113001 (2012).
- [51] X. Zhou, G. Liu, J. Yu, and W. Fan, Surface plasmon resonance-mediated photocatalysis by noble metal-based composites under visible light, *J. Mater. Chem.* **22**, 21337 (2012).
- [52] Y. V. Bludov, A. Ferreira, N. M. Peres, and M. I. Vasilevskiy, A primer on surface plasmon-polaritons in graphene, *Int. J. Mod. Phys. B* **27**, 1341001 (2013).
- [53] B. Zhao and Z. M. Zhang, Strong plasmonic coupling between graphene ribbon array and metal gratings, *ACS Photon.* **2**, 1611 (2015).
- [54] A. V. Zayats and I. I. Smolyaninov, Near-field photonics: Surface plasmon polaritons and localized surface plasmons, *J. Opt. A: Pure Appl. Opt.* **5**, S16 (2003).
- [55] A. V. Zayats, I. I. Smolyaninov, and A. A. Maradudin, Nanooptics of surface plasmon polaritons, *Phys. Rep.* **408**, 131 (2005).
- [56] K. M. Mayer and J. H. Hafner, Localized surface plasmon resonance sensors, *Chem. Rev.* **111**, 3828 (2011).
- [57] K. A. Willets and R. P. Van Duyne, Localized surface plasmon resonance spectroscopy and sensing, *Annu. Rev. Phys. Chem.* **58**, 267 (2007).
- [58] S. Unser, I. Bruzas, J. He, and L. Sagle, Localized surface plasmon resonance biosensing: Current challenges and approaches, *Sensors* **15**, 15684 (2015).
- [59] C. Zhang, Y. Lu, Y. Ni, M. Li, L. Mao, C. Liu, D. Zhang, H. Ming, and P. Wang, Plasmonic lasing of nanocavity embedding in metallic nanoantenna array, *Nano Lett.* **15**, 1382 (2015).
- [60] N. Maccaferri, A. Berger, S. Bonetti, V. Bonanni, M. Kataja, Q. H. Qin, S. van Dijken, Z. Pirzadeh, A. Dmitriev, J. Nogués *et al.*, Tuning the magneto-optical response of nanosize ferromagnetic ni disks using the phase of localized plasmons, *Phys. Rev. Lett.* **111**, 167401 (2013).
- [61] X. Pi and C. Delerue, Tight-binding calculations of the optical response of optimally p-doped si nanocrystals: A model for localized surface plasmon resonance, *Phys. Rev. Lett.* **111**, 177402 (2013).
- [62] P. Ben-Abdallah, S.-A. Biehs, and K. Joulain, Many-body radiative heat transfer theory, *Phys. Rev. Lett.* **107**, 114301 (2011).
- [63] S.-A. Biehs, R. Messina, P. S. Venkataram, A. W. Rodriguez, J. C. Cuevas, and P. Ben-Abdallah, Near-field radiative heat transfer in many-body systems, *Rev. Mod. Phys.* **93**, 025009 (2021).
- [64] D. Jin, T. Christensen, M. Soljačić, N. X. Fang, L. Lu, and X. Zhang, Infrared topological plasmons in graphene, *Phys. Rev. Lett.* **118**, 245301 (2017).
- [65] S. Yves, R. Fleury, T. Berthelot, M. Fink, F. Lemoult, and G. Lerosey, Crystalline metamaterials for topological properties at subwavelength scales, *Nat. Commun.* **8**, 16023 (2017).
- [66] X. Wu, Y. Meng, J. Tian, Y. Huang, H. Xiang, D. Han, and W. Wen, Direct observation of valley-polarized topological edge states in designer surface plasmon crystals, *Nat. Commun.* **8**, 1304 (2017).
- [67] M. S. Rider, Á. Buendía, D. R. Abujetas, P. A. Huidobro, J. A. Sánchez-Gil, and V. Giannini, Advances and prospects in topological nanoparticle photonics, *ACS Photon.* **9**, 1483 (2022).
- [68] C. Ling, M. Xiao, C. T. Chan, S. F. Yu, and K. H. Fung, Topological edge plasmon modes between diatomic chains of plasmonic nanoparticles, *Opt. Express* **23**, 2021 (2015).
- [69] M. Kim and J. Rho, Topological edge and corner states in a two-dimensional photonic Su-Schrieffer-Heeger lattice, *Nanophotonics* **9**, 3227 (2020).
- [70] A. Ott and S.-A. Biehs, Radiative heat flux through a topological Su-Schrieffer-Heeger chain of plasmonic nanoparticles, *Phys. Rev. B* **102**, 115417 (2020).
- [71] D. Han, Y. Lai, J. Zi, Z.-Q. Zhang, and C. T. Chan, Dirac spectra and edge states in honeycomb plasmonic lattices, *Phys. Rev. Lett.* **102**, 123904 (2009).
- [72] R. Li, M. R. Bourgeois, C. Cherqui, J. Guan, D. Wang, J. Hu, R. D. Schaller, G. C. Schatz, and T. W. Odom, Hierarchical hybridization in plasmonic honeycomb lattices, *Nano Lett.* **19**, 6435 (2019).
- [73] A. Ott and S.-A. Biehs, Topological near-field heat flow in a honeycomb lattice, *Int. J. Heat Mass Transfer* **190**, 122796 (2022).
- [74] Y. Zhang, R. P. Wu, L. Shi, and K. H. Fung, Second-order topological photonic modes in dipolar arrays, *ACS Photon.* **7**, 2002 (2020).
- [75] M. Proctor, M. Blanco de Paz, D. Bercioux, A. García-Etxarri, and P. Arroyo Huidobro, Higher-order topology in plasmonic kagome lattices, *Appl. Phys. Lett.* **118**, 091105 (2021).
- [76] Z. Mai, F. Lin, W. Pang, H. Xu, S. Tan, S. Fu, and Y. Li, Anderson localization in metallic nanoparticle arrays, *Opt. Express* **24**, 13210 (2016).

- [77] F. Rütting, Plasmons in disordered nanoparticle chains: Localization and transport, *Phys. Rev. B* **83**, 115447 (2011).
- [78] M. Petrov, Disorder-induced Purcell enhancement in nanoparticle chains, *Phys. Rev. A* **91**, 023821 (2015).
- [79] C. Forestiere, G. Miano, G. Rubinacci, and L. Dal Negro, Role of aperiodic order in the spectral, localization, and scaling properties of plasmon modes for the design of nanoparticle arrays, *Phys. Rev. B* **79**, 085404 (2009).
- [80] Z.-L. Deng, Z.-H. Li, J.-W. Dong, and H.-Z. Wang, In-plane plasmonic modes in a quasicrystalline array of metal nanoparticles, *Plasmonics* **6**, 507 (2011).
- [81] J.-W. Dong, K. H. Fung, C. T. Chan, and H.-Z. Wang, Localization characteristics of two-dimensional quasicrystals consisting of metal nanoparticles, *Phys. Rev. B* **80**, 155118 (2009).
- [82] L. Dal Negro and N.-N. Feng, Spectral gaps and mode localization in Fibonacci chains of metal nanoparticles, *Opt. Express* **15**, 14396 (2007).
- [83] J. B. Khurgin and G. Sun, Impact of disorder on surface plasmons in two-dimensional arrays of metal nanoparticles, *Appl. Phys. Lett.* **94**, 221111 (2009).
- [84] B. Wang and C. Zhao, Interferences and localization in disordered media with anisotropic structural correlations, *J. Appl. Phys.* **130**, 133101 (2021).
- [85] V. A. Markel, Anderson localization of polar eigenmodes in random planar composites, *J. Phys.: Condens. Matter* **18**, 11149 (2006).
- [86] Y. Wang, Y. Lu, J. Gao, K. Sun, Z. Jiao, H. Tang, and X. Jin, Quantum topological boundary states in quasicrystals, *Adv. Mater.* **31**, 1905624 (2019).
- [87] S. Law, R. Liu, and D. Wasserman, Doped semiconductors with band-edge plasma frequencies, *J. Vac. Sci. Technol. B* **32**, 052601 (2014).
- [88] R. P. H. Wu and H. C. Ong, Small mode volume topological photonic states in one-dimensional lattices with dipole-quadrupole interactions, *Phys. Rev. Res.* **4**, 023233 (2022).
- [89] L. Novotny and B. Hecht, *Principles of Nano-optics* (Cambridge University Press, Cambridge, 2012).
- [90] T. F. Allard and G. Weick, Quantum theory of plasmon polaritons in chains of metallic nanoparticles: From near-to far-field coupling regime, *Phys. Rev. B* **104**, 125434 (2021).
- [91] A. Moroz, Depolarization field of spheroidal particles, *J. Opt. Soc. Am. B* **26**, 517 (2009).
- [92] S. Y. Park and D. Stroud, Surface-plasmon dispersion relations in chains of metallic nanoparticles: An exact quasistatic calculation, *Phys. Rev. B* **69**, 125418 (2004).
- [93] B. X. Wang and C. Y. Zhao, Topological phonon polaritons in one-dimensional non-Hermitian silicon carbide nanoparticle chains, *Phys. Rev. B* **98**, 165435 (2018).
- [94] S. R. Poocek, P. A. Huidobro, and V. Giannini, Bulk-edge correspondence and long-range hopping in the topological plasmonic chain, *Nanophotonics* **8**, 1337 (2019).
- [95] S. Roy, T. Mishra, B. Tanatar, and S. Basu, Reentrant localization transition in a quasiperiodic chain, *Phys. Rev. Lett.* **126**, 106803 (2021).
- [96] T. Botzung, D. Hagenmüller, S. Schütz, J. Dubail, G. Pupillo, and J. Schachenmayer, Dark state semilocalization of quantum emitters in a cavity, *Phys. Rev. B* **102**, 144202 (2020).
- [97] T. F. Allard and G. Weick, Disorder-enhanced transport in a chain of lossy dipoles strongly coupled to cavity photons, *Phys. Rev. B* **106**, 245424 (2022).
- [98] K. Kawabata and S. Ryu, Nonunitary scaling theory of non-Hermitian localization, *Phys. Rev. Lett.* **126**, 166801 (2021).
- [99] J. Feinberg and A. Zee, Non-Hermitian localization and delocalization, *Phys. Rev. E* **59**, 6433 (1999).
- [100] X. Zhang, T. Zhang, M.-H. Lu, and Y.-F. Chen, A review on non-Hermitian skin effect, *Adv. Phys.: X* **7**, 2109431 (2022).
- [101] C. Lv, R. Zhang, Z. Zhai, and Q. Zhou, Curving the space by non-hermiticity, *Nat. Commun.* **13**, 2184 (2022).
- [102] R. E. Noskov, P. A. Belov, and Y. S. Kivshar, Subwavelength modulational instability and plasmon oscillons in nanoparticle arrays, *Phys. Rev. Lett.* **108**, 093901 (2012).
- [103] R. Noskov, P. Belov, and Y. Kivshar, Oscillons, solitons and domain walls in arrays of nonlinear plasmonic nanoparticles, *Sci. Rep.* **2**, 873 (2012).
- [104] R. E. Noskov, D. A. Smirnova, and Y. S. Kivshar, Plasmonic kinks and walking solitons in nonlinear lattices of metal nanoparticles, *Philos. Trans. R. Soc. A* **372**, 20140010 (2014).
- [105] J. Wiersig, Petermann factors and phase rigidities near exceptional points, *Phys. Rev. Res.* **5**, 033042 (2023).
- [106] G. Theodorou and M. H. Cohen, Extended states in a one-dimensional system with off-diagonal disorder, *Phys. Rev. B* **13**, 4597 (1976).
- [107] H. Fidder, J. Knoester, and D. A. Wiersma, Optical properties of disordered molecular aggregates: A numerical study, *J. Chem. Phys.* **95**, 7880 (1991).
- [108] Q. Tang and Y. He, Mobility edges in one-dimensional models with quasi-periodic disorder, *J. Phys.: Condens. Matter* **33**, 185505 (2021).
- [109] W. H. Weber and G. W. Ford, Propagation of optical excitations by dipolar interactions in metal nanoparticle chains, *Phys. Rev. B* **70**, 125429 (2004).
- [110] A. F. Koenderink and A. Polman, Complex response and polariton-like dispersion splitting in periodic metal nanoparticle chains, *Phys. Rev. B* **74**, 033402 (2006).
- [111] C. A. Downing, E. Mariani, and G. Weick, Retardation effects on the dispersion and propagation of plasmons in metallic nanoparticle chains, *J. Phys.: Condens. Matter* **30**, 025301 (2018).
- [112] A. Jagannathan, The Fibonacci quasicrystal: Case study of hidden dimensions and multifractality, *Rev. Mod. Phys.* **93**, 045001 (2021).
- [113] A. Alu and N. Engheta, Effect of small random disorders and imperfections on the performance of arrays of plasmonic nanoparticles, *New J. Phys.* **12**, 013015 (2010).